LRP 590/97 October 1997

Papers presented at the

7th European Fusion Theory Conference
Jülich, Germany, October 1997

by the CRPP Theory Group

LIST OF CONTENTS

Global Approach to the Spectral Problem of Microinstabilities in Tokamak Plasmas using a Gyrokinetic Model

S.Brunner, M.Fivaz and J.Vaclavik

Centre de Recherches en Physique des Plasmas

Association Euratom - Confédération Suisse

Ecole Polytechnique Fédérale de Lausanne/ PPB - CH-1015 Ecublens/Switzerland

Abstract

A gyrokinetic eigenvalue code has been developed for computing global ion temperature gradient (ITG) -related instabilities in tokamak configurations. Although trapped ion dynamics are not yet considered in this model, it contains full finite Larmor radius and finite orbit width effects of circulating ions. Non-adiabatic trapped electron dynamics are included through a bounce-averaged drift kinetic equation. Differences between the local ballooning approximation and the global approach are presented and discussed. The possible coupling between the trapped electron mode (TEM) and the toroidal-ITG mode is also investigated. Finally, the evolution of the spectrum of these different instabilities is studied for varying central negative magnetic shear configurations.

Introduction: For studying microinstabilities in tokamak-like plasmas, most linear kinetic studies were carried out for high toroidal wave numbers using the ballooning representation[1] which leads to a one-dimensional integral equation along the magnetic field lines. Except for very few cases, these calculations do not include a higher order WKB procedure for determining the radial structure. Thus these results usually stay local to a magnetic surface and there remains some questioning on the actual radial extent of these modes. For low toroidal wave numbers where the ballooning representation breaks down and the full two-dimensional problem cannot be reduced, very little linear computation has been carried out. This limit is of interest as it describes larger wavelength fluctuations which could lead to higher turbulent transport. Until recently the only published results from true global, linear computations came from a spectral code by Marchand, Tang and Rewoldt[2]. This model contains no finite Larmor radius (FLR) effects and is based on a second order expansion with respect to the radial excursion of trapped particles, which leads to spurious modes[3] and thus to a difficult search of physical eigenfrequencies. At the present state full non-linear simulations already exist[4][5], nonetheless there remains a need for global linear studies as they enable to determine more accurately the conditions of marginal stability and in this way, if possible, to find stable configurations. This has prompted us to undertake the development of a new, global, spectral gyrokinetic code. A summary of the present state physical model as well as of first results is given here. More details are found in Ref.[6].

Physical Model for the Spectral Approach

Geometry: At present the geometry of the system is still approximated by a large aspect ratio torus with circular, concentric magnetic surfaces. Therefore finite pressure effects such as the Shafranov shift are not taken into account. The safety factor profile $q_s(\rho)$, the ion and electron temperature profiles $T_{e,i}(\rho)$ as well as the density profile $N(\rho)$ are chosen arbitrarily and in this way are represented by simple polynomial functions of the radial variable ρ. Here (ρ, θ, φ) is the standard set of toroidal coordinates.

Kinetic equations: Although the basic mechanism of ITG instabilities can be described by fluid models, the more detailed behavior of these perturbations also contain specifically kinetic characters, such as wave-particle interaction (e.g. Landau damping) and FLR effects. In order to take them into account - this being essential if one is interested in determining accurately conditions of marginal stability- appropriate kinetic equations for each species must be considered. Assuming a collisionless plasma, these can be derived by reducing the Vlasov equation, linearized for electrostatic perturbations, using different scaling laws. In particular, as microinstabilities have low frequencies i.e. small compared to the cyclotron frequencies $\Omega_{e,i}$, one can for all particles carry out a gyroaveraging procedure.

In the case of **ions** the Larmor radius can be comparable or larger then the wavelengths perpendicular to the magnetic field, giving rise to the above mentioned FLR effects. The appropriate equation of motion is thus given by the gyrokinetic equation (GKE) [7]:

$$\left.\frac{D}{Dt}\right|_{u.t.GC} \tilde{g} = \left[\frac{\partial}{\partial t} + \vec{v}_{GC} \cdot \frac{\partial}{\partial \vec{R}}\right] \tilde{g} = -i\frac{q}{T} F_M(\omega - \omega^\star) < \phi >_g,$$

where $D/Dt|_{u.t.GC}$ stands for the total time derivative along the unperturbed trajectories $\vec{R}(t)$ of the guiding centers (GC), including drifts related to the gradient and curvature of the magnetic field. Furthermore, $\tilde{g}$ represents the fluctuating, non-adiabatic part of the particle distribution function written in gyro-center variables, F_M the local Maxwellian distribution of equilibrium, $\omega^\star$ the diamagnetic frequency related to the temperature and density inhomogeneities and $< \phi >_g$ the gyroaveraged electrostatic potential.

In first approximation the mobile **electrons** have been assumed to respond adiabatically to the low frequency microinstabilities and therefore to follow a Boltzmann distribution. However in the non-trivial tokamak geometry, the trapped electrons in fact have a toroidal precessional drift which can become comparable to the phase velocity of the perturbation. To take into account the resonances which may arise, a more detailed

description has been considered. As electrons have significantly smaller Larmor radii then ions for similar temperatures, FLR effects can usually be neglected (at least when studying ion-driven instabilities), so that the drift kinetic equation (DKE) instead of the GKE is sufficient. Furthermore, due to the high thermal velocity of these particles, this equation can be averaged over the periodic motion in the poloidal plane, giving rise to the so-called bounce-averaged DKE[8]:

$$\left.\frac{D}{Dt}\right|_{u.t.B} \tilde{g}_b = \left[\frac{\partial}{\partial t} + <\dot{\varphi}>_b \frac{\partial}{\partial \varphi}\right] \tilde{g}_b = -i\frac{q}{T} F_M(\omega - \omega^\star) < \phi >_b .$$

Here $D/Dt|_{u.t.B}$ stands for the total time derivative along the unperturbed trajectories of the banana (B) orbits, $\tilde{g}_b$ for the fluctuating, non-adiabatic part of the bounce-averaged GC distribution function, $<\dot{\varphi}>_b$ for the average toroidal precessional drift and $< \phi >_b$ for the bounce-averaged potential.

The equations of motion are solved by integrating along the unperturbed trajectories. In the case of ions the modulation of the magnetic field along the trajectory was neglected, so that in particular the dynamics of trapped ions was discarded. In its present state our model therefore still does not enable to describe trapped ion modes (TIM). In this context Fourier representation appears naturally as it enables to integrate explicitly the unknown potential ϕ. For example, when gyroaveraging the potential one obtains

$$< \phi >_g = < \int d\vec{k}\, \hat{\phi}\,(\vec{k},t)\, e^{i\vec{k}\cdot\vec{r}} >_g = \int d\vec{k}\, J_0\left(\frac{k_\perp v_\perp}{\Omega}\right) \hat{\phi}\,(\vec{k},t) e^{i\vec{k}\cdot\vec{R}},$$

where J_0 is the zero order Bessel function containing the full FLR effects and having used the relation $\vec{R} = \vec{r} + \vec{v} \times \vec{e}_{||}\,/\Omega$ between the GC and particle position. In fact, instead of a decomposition into plane waves, a Fourier representation in terms of toroidal wave components was chosen as it is more adapted to the geometry of the system:

$$\phi(\rho,\theta,\varphi;t) = \sum_{(\kappa,m)} \hat{\phi}_{(\kappa,m)} \exp i(\kappa\rho + m\theta + n\varphi - \omega t),$$

where κ is a radial, m a poloidal and n the fixed toroidal wave number. Note that a Fourier series decomposition instead of a Fourier transform is considered not only in the periodic direction θ but also along the radial coordinate ρ, this being justified by the finite dimension of the system. The fixed frequency is noted ω.

Eigenvalue equation: The equations of motion are completed with a relation for ϕ. This is provided by the quasineutrality equation (justified when studying low frequency microinstabilities), which leads to the actual eigenvalue equation for (ω, ϕ). It turns out

to be advantageous to solve this eigenvalue problem staying in the discrete Fourier space (κ, m). Indeed, the equation is then naturally discretized and contains no singularity as the one appearing in the kernel of the integral equation when solving in the continuous configuration space (ρ, θ). The eigenvalue problem can formally be written in matrix form:

$$\overleftrightarrow{M}(\omega)\,\vec{\phi} = 0.$$

This is not a standard problem as the matrix $\overleftrightarrow{M}$ has an intricate dependence in the eigenvalue ω. The characteristic equation for ω:

$$D(\omega) = \det \overleftrightarrow{M}(\omega) = 0, \qquad \omega \text{ complex},$$

is solved by taking advantage of the analyticity of $D(\omega)$ and using a practical method proposed by Davies[9]. By sampling $D(\omega)$ along a closed curve in the complex frequency plane, this approach allows not only to find the number of enclosed zeros using the principle of argument (Nyquist), but the value itself of these roots with great accuracy. In this way the full unstable spectrum of a given system can be computed quite effectively.

Results

Benchmarking with time evolution PIC code: The spectral code has been extensively benchmarked against another global, linear gyrokinetic code developed simultaneously at the CRPP, based on a time evolution particle in cell (PIC) method[10][11]. In the regime where trapped ion dynamics (contained in the PIC model) are not important, i.e. for frequencies above the average ion bounce frequency, and for not too short wavelengths (PIC model is only valid to second order in Larmor), comparisons have shown very good agreement. Details of this validation can be found in Ref.[12].

Comparison with local ballooning calculations: Results from the global spectral code have also been compared to those obtained by Dong et al.[13] applying the local ballooning approximation to the same physical model. In this case only the adiabatic response of trapped electrons is taken into account so that the instabilities are essentially toroidal-ITG. To carry out such a comparison, the profiles for the global code must be chosen such that they match the local ballooning parameters on a reference magnetic surface. Here these parameters are given by the safety factor q_s, the temperature ratio $\tau = T_e/T_i$, $\epsilon_n = L_n/R$ =characteristic length of density/ major radius, $\eta_i = L_n/L_{T_i}$ =charac.length of density/ charac.length of ion temperature and the normalized poloidal mode number

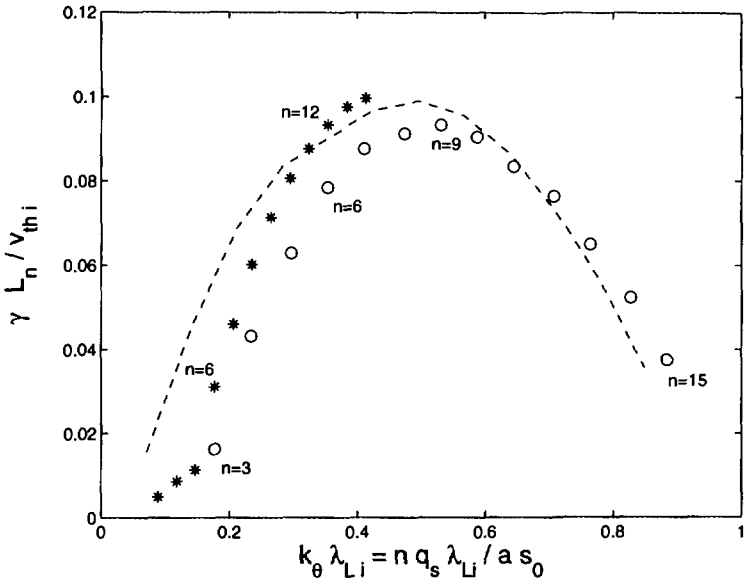

Figure 1: Growth rate γ as a function of $k_\theta \lambda_{Li}$ (only adiabatic response of electrons). Circles and stars represent global results for $a/\lambda_{Li} = 56.5$ and $a/\lambda_{Li} = 113.0$ respectively, a being the minor radius of the plasma. Labels below the circles and above the stars indicate the corresponding toroidal wave number. Ballooning results are reported here with a dashed line.

$\tilde{k_\theta} = nq_s\lambda_{Li}/\rho_0$, where λ_{Li} is the average ion Larmor radius on the reference magnetic surface $\rho = \rho_0$. Note that both, a high temperature plasma with a perturbation having low toroidal mode number n, or a low temperature and high n, can lead to a same value $\tilde{k_\theta}$ and thus be iso-dynamical with respect to the local ballooning calculation. Fig.1 presents the growth rates obtained when carrying out such a comparison along an n-scan. A hot as well as a cold plasma scenario have been considered when running the global code and in both cases the corresponding results indeed join the local ones for sufficiently high toroidal mode numbers, i.e. $n \gtrsim 10$. Ballooning results are from Fig.3 of Ref.[13]. The typical role over of the growth rate around $\tilde{k_\theta} \simeq 0.5$ is the consequence of FLR effects.

Effect of trapped electrons on the toroidal-ITG: The effect of non-adiabatic trapped electron dynamics is essentially twofold. In case of a flat density profile it simply strengthens the growth rate of the toroidal-ITG instability, which thus keeps its dominantly ion driven character. For non-flat density profiles (low values of ϵ_n and η_i) the toroidal-ITG can either couple and convert to, or simply be taken over by a trapped electron mode (TEM). This TEM may remain unstable down to flat ion temperature profiles, thus effectively removing the threshold on η_i predicted for the pure toroidal-ITG when only adiabatic electrons are considered. In this way our global results qualitatively

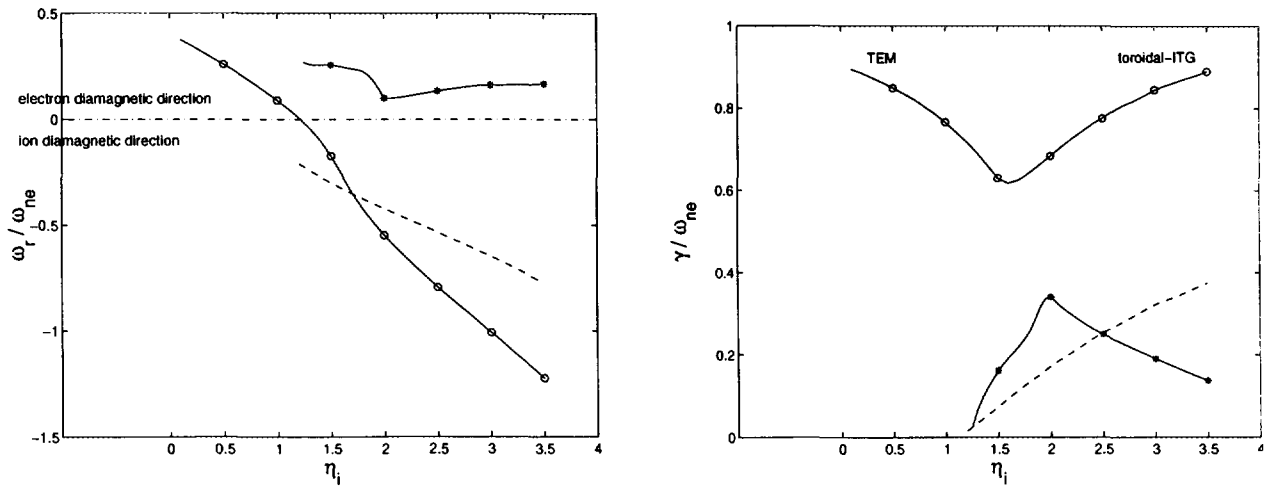

Figure 2: Real frequencies ω_r and growth rates γ of the most unstable eigenmodes as a function of η_i holding in particular $\epsilon_n = 0.2$=const and $\eta_e = 2$ =const, computed with non-adiabatic trapped electrons (full lines). For $\eta_i \lesssim 1$ the toroidal-ITG converts to a predominantly TEM (mode 1) and starts to propagate in the electron instead of the ion diamagnetic direction. A weaker instability propagating essentially in the electron diamagnetic direction (mode 2) is also present. For comparison, results with only adiabatic electrons are reproduced with dashed lines. Note how non-adiabatic trapped electron dynamics have removed the threshold on η_i.

confirm the picture given by Romanelli and Briguglio [14] solving a local dispersion relation. As an illustration, results of an η_i-scan are presented in Fig.2.

Negative shear scan: The global spectral code has been applied for studying the stabilizing effect of negative magnetic shear. Motivation for such studies come from experimental evidence on different tokamaks[15][16][17] of the formation of a transport barrier in regions of shear reversal accompanied by a reduction in core fluctuation amplitudes. Fig.3 presents the results of such a shear scan having fixed $n = 10$ and the profiles such that $\tau = 1$, $\epsilon_n = 0.25$, $\eta_i = \eta_e = 2.5$, $\tilde{k_\theta}$= 0.35, $\alpha_b = 45\%$ (fraction of trapped particles) on the magnetic surface $\rho = \rho_0$ where the modes tend to be centered (steepest gradients). The safety factor profile is varied such that $q_s(\rho_0) = 1.5$ is held fixed while shear varies from $\hat{s}\ (\rho_0) = +1$ to -1. For positive values of shear the spectrum contains eigenmodes propagating in the ion diamagnetic direction, i.e. having a dominantly toroidal-ITG character, as well as instabilities propagating in the electron diamagnetic direction, i.e. having essentially a TEM character. In this case, the TEM's are completely suppressed at negative shear $\hat{s}$= -1, while the toroidal-ITG modes are still present, their growth rate being nonetheless attenuated by a factor ~ 4 with respect

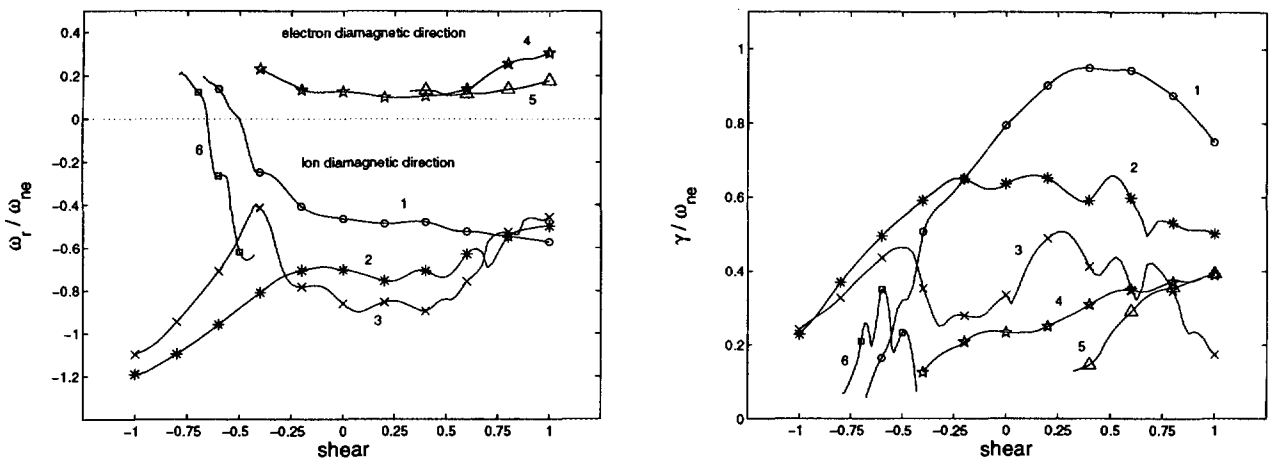

Figure 3: Real frequencies ω_r and growth rates γ as a function of shear $\hat{s}$ for a sampling of unstable eigenmodes, non-adiabatic trapped electron dynamics being taken into account. For $\hat{s}= +1.0$ the unstable spectrum contains simultaneously positive and negative frequencies. At $\hat{s}= -1.0$ only the ITG-type modes remain destabilized, however with a significantly reduced growth rate compared with the highest one around $\hat{s}= +0.5$.

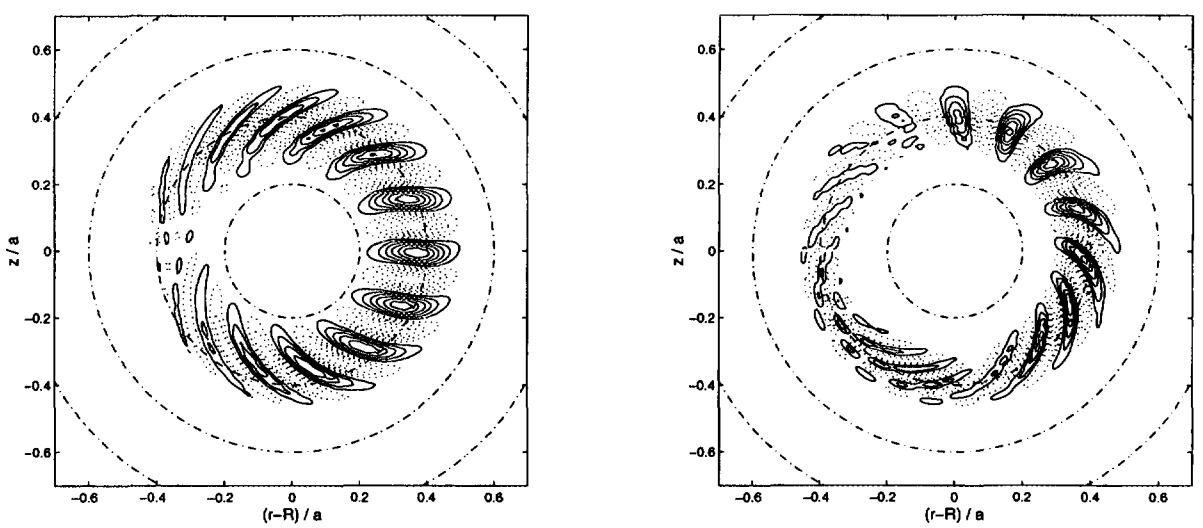

a.) $\hat{s}= +1.$ e.) $\hat{s}= -1.$

Figure 4: Mode structures of most unstable toroidal-ITG-type eigenmodes along shear scan $\hat{s}= +1. \ldots . - 1.$

to $\hat{s}$= 0.5. Negative shear stabilizes the toroidal-ITG by twisting the convective cells more rapidly into a vertical position where they are less effectively driven[18]. This appears clearly in the poloidal mode structures of Fig.4 (axis of symmetry on the left). The TEM's are stabilized by reversal of the average toroidal precessional drift of the trapped particles. Thus realistic negative magnetic shear alone does not seem to be sufficient to explain the dramatic improvement of confinement in negative central shear discharges. Experimental results[16] point towards the $\vec{E} \times \vec{B}$ flow shear for being responsible for the full stabilization of microinstabilities[19].

References

[1] J.W.Connor, R.J.Hastie, and J.B.Taylor, Physical Review Letters **40**, 396 (1978).

[2] R.Marchand, W.M.Tang, and G.Rewoldt, Physics of Fluids **23**, 1164 (1980).

[3] W.M.Tang and G.Rewoldt, Physics of Fluids B **5**, 2451 (1993).

[4] S.E.Parker, W.W.Lee, and R.A.Santoro, Physical Review Letters **71**, 2042 (1993).

[5] M.Kotschenreuther, W.Dorland, M.A.Beer, and G.W.Hammett, Physics of Plasmas **2**, 2381 (1995).

[6] S.Brunner, Ph.D. thesis, Ecole Polytechnique Fédérale de Lausanne, 1997.

[7] P.J.Catto, Plasma Physics **20**, 719 (1978).

[8] M.Rosenbluth and M.L.Sloan, Physics of Fluids **14**, 1725 (1971).

[9] B.Davies, Journal of Computational Physics **66**, 36 (1986).

[10] M.Fivaz *et al.*, Physical Review Letters **78**, 3471 (1997).

[11] M.Fivaz, Ph.D. thesis, Ecole Polytechnique Fédérale de Lausanne, 1997.

[12] S.Brunner *et al.*, in *Theory of Fusion Plasmas, Int. Workshop, Varenna, August 1996* (Editrice Compositori, Societa Italiana di Fisica, Bologna, 1997), p. 101.

[13] J.Q.Dong, W.Horton, and J.Y.Kim, Physics of Fluids B **4**, 1867 (1992).

[14] F.Romanelli and S.Briguglio, Physics of Fluids B **2**, 754 (1990).

[15] F.M.Levinton *et al.*, Physical Review Letters **75**, 4417 (1995).

[16] L.L.Lao *et al.*, Physics of Plasmas **3**, 1951 (1996).

[17] Y.Neyatani and the JT-60 Team, Plasma Physics and Controlled Fusion **38**, A181 (1996).

[18] T.M.Antonsen Jr. *et al.*, Physics of Plasmas **3**, 2221 (1996).

[19] T.S.Hahm and K.H.Burrell, Physics of Plasmas **2**, 1648 (1995).

CH9800022

Study of second stability for ITG modes

M. Fivaz, O. Sauter, K. Appert, S. Brunner, T. M. Tran, J. Vaclavik

Centre de Recherches en Physique des Plasmas, Association Euratom-Confédération Suisse
EPFL, PPB, 1015 Lausanne, Switzerland

Abstract The second stability regime for ion-temperature-gradient (ITG) modes is studied in details with a global linear gyrokinetic Particle-In-Cell code which takes the full toroidal MHD equilibrium data. The trapped-ion and the toroidal ITG regimes are explored. We perform simultaneous ideal MHD stability computations for both kink ($n = 1$) and ballooning ($n = \infty$) modes. We use the results to find partially optimized configurations that are stable to ideal MHD modes and where the ITG modes are stable or have very low growth rates. Such configurations are expected to have very low level of ITG-induced transport.

Introduction. Unstable ITG modes are now commonly held responsible for anomalous ion heat transport in tokamaks. The ion temperature gradient provides free energy to the instability and the magnetic field gradient provides an efficient destabilizing mechanism on the outer side of the torus. These modes are stable when the ion temperature gradient is below a critical values (first stability regime). At high pressure, the plasma diamagnetism can reduce of even reverse the gradient of the equilibrium magnetic field, which then becomes favorable everywhere in the plasma; the ITG modes can then be completely stabilized [1] in what can be called a second stability regime. This effect is sometimes referred to as "Shafranov-shift stabilization".

Previous calculation [2] [3] [4] are undetailed and were done using the ballooning approximation and (except [2]) with the "$s - \alpha$" approximation to the equilibrium magnetic field, a high aspect ratio, circular shifted magnetic surface approximation. The ballooning approximation, though, breaks down at low n or low magnetic shear, and cannot describe slab-like modes that are not localized on the outer side of the torus, i.e. that do not "balloon". The "s-α" model also breaks down at realistic aspect ratio and in non-circular plasmas.

We study here in detail the conditions that lead to the second stability for ITG modes, using a global approach (no ballooning approximation) and the full MHD equilibrium data. We focus on cases where a low magnetic shear stabilizes the local, short wavelength MHD ballooning modes. We use the code GYGLES (GYrokinetic Global LinEar Solver)[5] [6], which uses a radially global approach in toroidal geometry. The simulation model is based on the linear gyrokinetic equations for the ions in which the full guiding center trajectories are kept. We assume the electrons to respond adiabatically and the equilibrium perturbation to be electrostatic and quasineutral. The gyrokinetic equations are linearized around an equilibrium local Maxwellian distribution function. The code uses a Particle-In-Cell method with finite elements defined in magnetic coordinates. The code can simulate routinely global modes of all (very short to very long) toroidal wavelengths, can treat realistic (MHD) equilibria of any

Global parameters	$R_0 = 3$ m, $a/R_0 = 1/.36$, elong. 1.6, triang. .3, vac. field $B_0(R_0) = 3$ T, $\rho \approx 4.8$ mm (deuterium)
Temperatures	$\frac{T_i}{dT_i/ds} = -\frac{1}{2}\kappa_T \left(1 + \cos\left[\frac{\pi}{2}\frac{s-s_0}{\Delta s}\right]\right)$ for $\lvert s - s_0\rvert < 2\Delta s$, 0 elsewhere $\kappa_T = \frac{1}{\Delta s}\log(T_{mul})$, $s_0 = .6$, $\Delta s = 0.1$, $T_i(s_0) = 10$ Kev, $T_e = T_i$
Density profile	$n_i(s) = n_0(1 - s^2)^4$
Norm. current density	$\hat{I}^*(s) = j_0(1 - s^2) + j_a \exp\left[-\frac{(s-s_0)^2}{\Delta s_j^2}\right]$ $j_a = T_{mul} * (.14 * j_0 + .24)$, $\Delta s_j = 0.15$
Scan parameters	$j_0 \in [.8, 100]$, $T_{mul} \in [1.1, 1.8]$
Parameters at $s = s_0$	$R_0/L_T \equiv \kappa_T R_0/a$, $R_0/L_n = 2.8$, $q = 1.5$, shear $\hat{s} \approx 0.2$

Table 1: *Specification of the equilibria studied.*

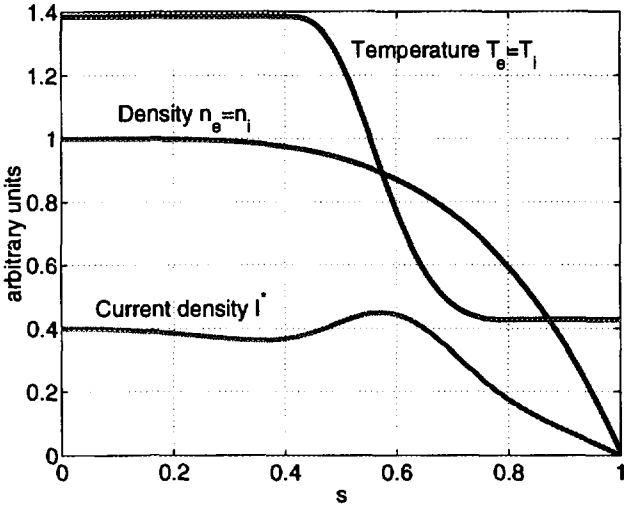

Figure 1: *Profiles from table (1).*

size and runs on a massively parallel computer.
The inclusion of electromagnetic perturbations can affect (usually stabilize further) ITG modes at high β [7] [4] [8] [9]. This effect is not included here; we focus rather on the stabilizing effect of the modification of the equilibrium at high β using realistic (MHD) equilibrium magnetic structure.

Parametric study. We introduce a radial variable $s = \sqrt{\Psi/\Psi_a}$, where Ψ is the equilibrium poloidal magnetic flux and Ψ_a its value at the plasma boundary, the plasma major and minor radii R_0 and a and the normalized temperature gradient $\frac{R_0}{L_T} \equiv \frac{R_0}{a}\frac{\partial T/\partial s}{T}$. Locally on the outer plasma mid-plane, one can derive from the MHD equilibrium condition a criterion for magnetic gradient reversal:

$$\alpha \equiv -\mu_0 \frac{R}{B_t^2}\frac{\partial p}{\partial R} > 1$$

The reversal parameter α is such that $\alpha = 0$ at low pressure and $\alpha > 1$ when the magnetic field gradient is reversed on the outer mid-plane. It is therefore a local parameter characterizing the magnetic field gradient at the most unfavorable point. It differs by a factor q^2 from the usual α parameter from "$s - \alpha$" equilibria and that is important in MHD ballooning computations. The table (1) defines a set of JET-size equilibria where the profile of R_0/L_T is inspired by a high-confinement JT60-U discharge [10] and peaks at a given magnetic surface at $s = s_0$, thus confining the unstable modes around that surface. In what follows, R_0/L_T and α refer to their values at $s = s_0$. Both α and R_0/L_T can be chosen by varying the parameters j_0 and T_{mul}. In the region where the modes lie, the safety factor does not depend on R_0/L_T and α. The magnetic shear $\hat{s}$ is low, $0 < \hat{s} < 0.2$, where the modes lie. This has the effect that all these equilibria are stable to MHD ballooning modes; in particular, equilibria with high pressure gradients lie in the second stability zone [12].
We use this set to do a generic study of ITG stability as a function of R_0/L_T and α at fixed safety factor profile, in both the regimes of toroidal ITG (high toroidal mode number n, mode frequency $\equiv \omega > \omega_b \equiv$ trapped-ion bounce frequency) and the trapped-ion regimes (low n, $\omega < \omega_b$).
The profiles of the surface-averaged current $I^*(s)$ and of the pressure $p(s) = n_i(s)\,(T_e(s) + T_i(s))$ are first used to solve the Grad-Shafranov equation with the code CHEASE [11], yielding the magnetic field structure that is then used by GYGLES to compute ITG stability.

Results. Figure (2) shows the contours of the growth rates obtained for $n = 12$ and $n = 48$ in the (α,R_0/L_T) plane. The frequency of these modes increases with R_0/L_T and with n, while

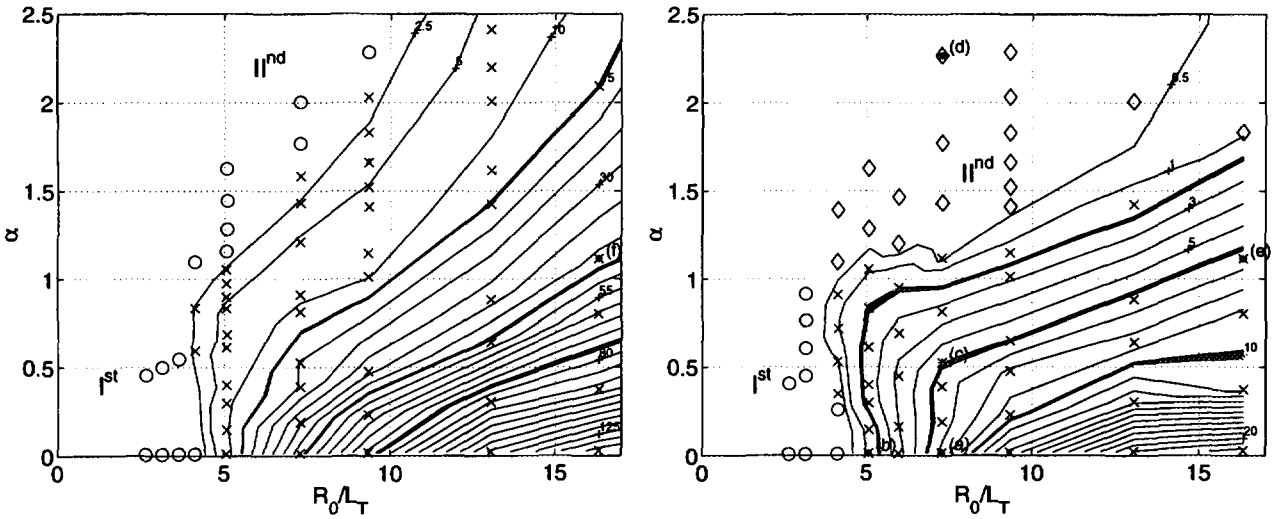

Figure 2: *Contours of the growth rate (in kHz). Left: n=48, Toroidal ITG regime. Right: n=12, Trapped-ion mode regime. The crosses (o), circles (x) and diamond (◇) represent respectively equilibria that were found stable, unstable to toroidal modes, and very weakly unstable to slab-like modes.*

the ion bounce frequency ω_b is fixed. As a results, the $n = 12$ modes are in the trapped-ion regime with $\omega < \omega_b$, except at high R_0/L_T, where they have a small toroidal ITG character. Conversely, the $n = 48$ modes are in the toroidal ITG regime, except at very low values of R_0/L_T.

We call "first stability zone" the stable zone, marked "I^{st}" on Fig. 2, that lies below a critical temperature gradient. Above this gradient, the mode is stabilized for increasing α as ∇B decreases and is reversed for $\alpha \geq 1$, leading to the "second stability zone" for ITG modes, marked "II^{nd}" on the same figure. In the toroidal ITG regime, these equilibria are fully stable, while in the trapped-ion regime, a weakly unstable slab-like ITG mode remains. The second stability regime is therefore strictly stable to toroidicity-related modes only (at least at low shear), but the slab-like modes are not expected to cause much anomalous transport, as they are radially narrow and very weakly unstable. The structure of the eigenmodes marked (a) (a trapped-ion mode) and (d) (a slab-like ITG mode) on Fig. (2), are shown in Fig. (3). The contours of growth rates corresponding to mixing-length estimates of the heat diffusivity $\chi_\perp = 1$, 3 and 5 m^2/s are shown in bold in Fig. (2). While these values should not be taken as more than rough estimates, they show that the scan covers most of the experimentally relevant range of $0.1 - 10$ m^2/s.

MHD stability calculations. The CHEASE code was used to compute the stability of MHD ballooning modes. All the equilibria presented here are stable to these modes at the surface $s = s_0$; this was achieved by lowering the magnetic shear to a $0 < \hat{s} < 0.2$, so pushing the equilibria with high values of α into the second stability regime for ballooning modes. Kinetic effects on these modes were not considered [4]. This demonstrates the existence of a simultaneous second stability regime for ITG modes and for MHD ballooning modes. The code ERATO [13] was used to compute the stability to kink modes. The points (a), (c) and (e) on Fig. (2), the latter at $\alpha = 1.1$, are stable to the global n=1 kink mode; stability at values of α that are roughly 50% higher is obtained if an ideal wall is added at $r_{wall}/a = 1.2$, assuming sufficient toroidal rotation and wall stabilization effect. In particular, the equilibrium corresponding to the point at $R_0/L_T = 16.3$ and $\alpha = 1.8$ is MHD-stable with an ideal wall and is only weakly unstable to ITG modes; it is the most interesting global case in our scan. The corresponding profiles are those of Fig. (1).

Conclusions. We studied the simultaneous access to second stability for ITG modes and for

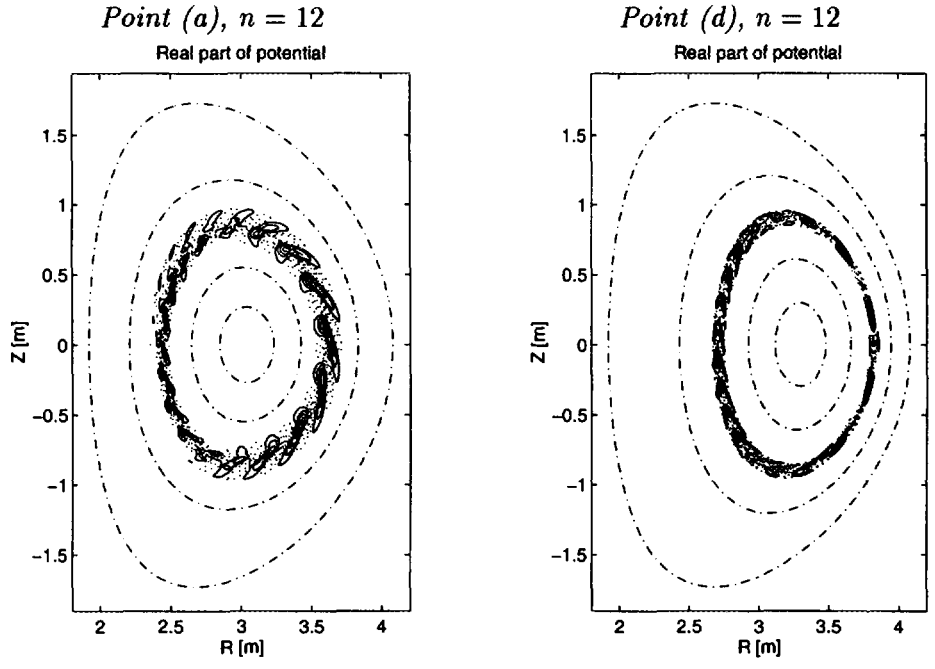

Figure 3: *Eigenmodes corresponding to the points (a) and (d) shown in Fig. (2).*

ballooning modes. The MHD ballooning modes are stabilized by low shear on the surface of interest in all the configurations presented. The stabilization of ITG modes is well described by the local magnetic field gradient reversal parameter α, and any ITG-induced transport should be strongly reduced for $\alpha \approx 1$.
Global kink modes are stable without ideal wall up to relatively high values of α, $\alpha = 1.1$ for $R_0/L_T = 16.3$. When a ideal wall at r_{wall}/a=1.2 is included, one obtains stability at $\alpha = 1.8$ for the same temperature gradient. This equilibrium has therefore good MHD properties and should have sustainable ITG transport ($\chi_\perp \approx 1$ m^2/s, Fig. (2)) while its temperature gradient is three times higher than the critical gradient at low β. By optimizing the plasma shape and profiles, we expect to find in the near future improved optimized high-performance configurations that are stable to all ideal MHD modes and stable or weakly unstable only to global ITG modes.
We finally note that some experimental discharges seem to have accessed $\alpha \approx 1$ [6].
This research work was supported in part by the Swiss National Science Foundation and the Cray-EPFL PATP project. The computations were done on the Cray-T3D parallel supercomputer of the EPFL-PATP.

References

[1] M. Fivaz *et al.*, Phys. Rev. Lett. **78**, 3471 (1997).
[2] G. Rewoldt, W. M. Tang, and M. S. Chance, Phys. Fluids **25**, 480 (1982).
[3] X. Q. Xu and N. M. Rosenbluth, Phys. Fluids B **3**, 627 (1991).
[4] M. Yamagiwa, A. Hirose, and M. Elia, Plasma Phys. Control. Fusion **39**, 531 (1997).
[5] M. Fivaz *et al.*, submitted to Computer Physics Communications **0**, 0 (1997).
[6] M. Fivaz, PhD thesis No. 1692, Ecole polytechnique Fédérale de Lausanne, Switzerland, 1997.
[7] J. Y. Kim, W. Horton, and J. Q. Dong, Phys. Fluids B **5**, 4030 (1993).
[8] R. R. Domingez and R. W. Moore, Nucl. Fusion **26**, 85 (1986).
[9] A. Jarmen, P. Anderson, and J. Weiland, Nucl. Fusion **27**, 941 (1987).
[10] Y. Neyatani and the JT60-Team, Plas. Phys. Control. Fusion **38**, A181 (1996).
[11] H. Lütjens, A. Bondeson, and O. Sauter, Comput. Phys. Commun. **97**, 219 (1996).
[12] D. Lortz and J. Nührenberg, Phys. Lett. **68A**, 49 (1978).
[13] R. Gruber *et al.*, Comput. Phys. Commun. **21**, 323 (1981).

CH9800023

Simulations of Ion-Temperature-Gradient modes in helical symmetry

L. Villard, M. Fivaz, J. Vaclavik
Centre de Recherches en Physique des Plasmas, Association Euratom - Confédération Suisse, Ecole Polytechnique Fédérale de Lausanne

Abstract. We present the first simulations of Ion Temperature Gradient (ITG) modes in straight helical configurations. A linear particle-in-cell gyrokinetic global code initially developed for toroidal axisymmetric geometry [1, 2] has been modified to treat the case of helical symmetry. The model is based on gyrokinetic ions, adiabatic electrons and electrostatic quasineutral perturbations. The code simulates the full plasma cross-section. The potential is represented on a magnetic coordinate system and discretized with finite elements. Analytical extraction of the fast poloidal variation is done on a straight field line coordinate, allowing a speedup of one or two orders of magnitude. A $l = 1$ vacuum field configurations is studied. The very low shear and small ∇B drifts imply that for a wide range of parameters the most unstable ITG modes are "slab-like".

Introduction. Anomalous transport in magnetically confined plasmas is widely believed to be attributed to micro-instabilities of low frequency drift-wave type. Over the past years the efforts in the theoretical analysis have focused on axisymmetric configurations of the tokamak type. In contrast, very little has been done for stellarators: previous works on drift waves [3] - [6] have so far been limited to simple cold ion electrostatic models with local and ballooning approximations. The present work is the first that addresses the question of Ion-Temperature-Gradient (ITG) modes in helical geometry. The specific objective is to get an understanding of ITG modes and to compare with the tokamak results. The longer term goal is to understand whether or not transport in stellarators, if determined by such micro-instabilities, can be different from that in a tokamak.

Helical Geometry. In this paper we shall consider helical symmetry (i.e. straight stellarators). Let r, φ, z be the cylindrical coordinates. Helical symmetry implies that all scalar equilibrium fields can be expressed as functions of two variables: r and $\zeta = \varphi - hz$, where h is the helicity. A toroidal configuration of N_{per} field periods and major radius R_0 is thus modeled by a helicity $h = N_{per}/R_0$. Let us introduce the following coordinates: a helical system (x', y') with $x' = r\cos\zeta$, $y' = r\sin\zeta$, and a magnetic coordinate system (s, θ) with $s = ((\psi - \psi_{min})/(\psi_{max} - \psi_{min}))^{1/2}$, where ψ is the helical flux, $\theta = \arctan(y'/(x' - x'_m))$, where the magnetic axis position is $(x' = x'_m, y' = 0)$. In addition to the "poloidal" coordinate θ, we introduce the straight field line coordinate χ

$$\tilde{q} = \frac{h}{2\pi}\int_0^{2\pi} \frac{\mathbf{B}\cdot\nabla z}{\mathbf{B}\cdot\nabla\theta} d\theta \qquad \chi = \frac{h}{\tilde{q}}\int_0^{\theta} \frac{\mathbf{B}\cdot\nabla z}{\mathbf{B}\cdot\nabla\theta} d\theta \tag{1}$$

where the integrals are on a $\psi = const$ surface. Note that with this definition the rotational transform per helical period length $L = 2\pi/h$ is $\iota = 1/\tilde{q} + 1$.

The equilibrium magnetic field is given by the representation

$$\mathbf{B} = F\mathbf{u} + \nabla\psi \times \mathbf{u} \qquad \mathbf{u} = (hr\mathbf{e}_\varphi + \mathbf{e}_z)/(1 + h^2r^2) \tag{2}$$

with F a function of ψ so that $\mathbf{B}$ satisfies the helical symmetry and $\nabla\cdot\mathbf{B} = 0$. In this

paper we shall restrict ourselves to vacuum fields. They can be expressed as

$$\psi = \frac{1}{2}Fhr^2 - r\sum_l b_l I_l'(lhr)\cos(l\zeta) \tag{3}$$

where F is a constant and I_l is the modified Bessel function of order l.

Gyrokinetic model. The plasma ions are described with a linearized gyrokinetic model with the usual ordering: $\omega/\Omega \sim k_\parallel/k_\perp \sim e\phi/T_e \sim \rho/L_n \sim \rho/L_T \sim \mathcal{O}(\epsilon_g)$, where ρ is the ion Larmor radius, Ω is the ion cyclotron frequency, $L_E^{-1} = |\nabla \ln E|, E = n_0, T$. Another small parameter is $\rho/L_B \sim \mathcal{O}(\epsilon_B)$, with $L_B = B/|\nabla B|$. Consistent with the gyrokinetic ordering, the perturbations of interest have $k_\parallel << k_\perp$. We use this property to extract the poloidal phase variation of the mode

$$f(\mathbf{x},t) = \tilde{f}(s,\theta,t)e^{iS} \qquad \phi(\mathbf{x},t) = \tilde{\phi}(s,\theta,t)e^{iS} \qquad S(s,\theta,z) = m_0\chi(s_0,\theta) + kz - \omega_0 t \tag{4}$$

where $k = hn/N_{per}$, n is the "helical" mode number, the magnetic surface $s = s_0$ is chosen near the expected maximum mode amplitude, m_0 is an integer close to $-n\tilde{q}_0/N_{per}$, and $\tilde{q}_0 = \tilde{q}(s_0)$. Note that a perturbation having a single Fourier component m in the straight field line poloidal angle χ has

$$k_{\parallel,m} = \frac{B_z}{B}h(\frac{m}{\tilde{q}} + \frac{n}{N_{per}}). \tag{5}$$

The transformed quantities $(\tilde{\phi}, \tilde{f})$ are expected to have a slow poloidal variation, the fast variation having been extracted by the phase factor. This technique will allow us to study high n modes with the same computational performance as low n modes. The quantity ω_0 is not the eigenfrequency but serves to shift the simulated frequencies; this is particularly useful to study modes near the marginal stability with $\gamma << \omega$.

The unperturbed trajectories of the guiding centres (GC) have three constants of motion: the kinetic energy, the magnetic moment and the helical canonical momentum $\Psi_0 = \psi + (m_i/q_i)v_\parallel F/B$. The equilibrium ion distribution function f_0 is assumed isotropic Maxwellian with density and temperature constant on a magnetic surface. The perturbed distribution function is evolved along the unperturbed trajectories. The electrons are assumed to respond adiabatically. The quasi-neutrality condition, in which the polarization density is approximated by a differential expression valid up to $(k_\perp\rho)^2$, close the system of equations:

$$\frac{d\mathbf{R}}{dt} = v_\parallel \mathbf{e}_\parallel + \frac{v_\parallel^2 + v_\perp^2/2}{\Omega}\mathbf{e}_\parallel \times \nabla \ln B, \quad \frac{dv_\parallel}{dt} = \frac{1}{2}v_\perp^2 \nabla\cdot\mathbf{e}_\parallel, \quad \frac{dv_\perp}{dt} = -\frac{1}{2}v_\perp v_\parallel \nabla\cdot\mathbf{e}_\parallel \tag{6}$$

$$\frac{d\tilde{f}}{dt} + i\frac{dS}{dt}\tilde{f} = \frac{-\tilde{\mathbf{E}}}{B}\cdot\left((\mathbf{e}_\parallel \times \nabla\psi)\frac{\partial f_0}{\partial \psi} + \Omega\mathbf{e}_\parallel\frac{\partial f_0}{\partial v_\parallel} + (\mathbf{e}_\parallel \times \nabla \ln B)\left(v_\parallel\frac{\partial f_0}{\partial v_\parallel} + \frac{1}{2}v_\perp\frac{\partial f_0}{\partial v_\perp}\right)\right) \tag{7}$$

$$\tilde{\mathbf{E}}(\mathbf{R}, v_\perp) = -\frac{1}{2\pi}\int \mathcal{G}\tilde{\phi}(\mathbf{x})\delta(\mathbf{x} - \mathbf{R} + \boldsymbol{\rho})e^{i(S(\mathbf{x})-S(\mathbf{R}))}d\mathbf{x}d\alpha \tag{8}$$

$$\frac{n_0 e}{T_e}\tilde{\phi}(\mathbf{x}) - \mathcal{G}_\perp\cdot\frac{n_0}{B\Omega}\mathcal{G}_\perp\tilde{\phi}(\mathbf{x}) = \int \tilde{f}(\mathbf{R}, v_\parallel, v_\perp)\delta(\mathbf{R} - \mathbf{x} + \boldsymbol{\rho})e^{i(S(\mathbf{R})-S(\mathbf{x}))}d\mathbf{R}d\mathbf{v} \tag{9}$$

where $\mathcal{G} = (i\nabla S + \nabla)$.

The distribution function $\tilde{f}$ is discretized in a 4-D reduced phase space $(x', y', v_{||}, v_{\perp})$. The potential $\tilde{\phi}$ is discretized with quadratic spline finite elements in (s, θ). The new version of the code has been benchmarked against the axisymmetric version by considering a straight field configuration ($T = B_0 = const, b_l = 0$). We have checked that the results coincide and are independent of the helicity h. Convergence with the timestep, the mesh and the number of particles, and power consistency have been demonstrated.

Results. We consider the following $l = 1$ configuration: $F = 1T$, $b_1 = 0.5T$, $a = 0.5m$, $h = 1m^{-1}$, flat density, $T_e = T_i$, $d\ln T_i/ds$ profile peaking at $s = s_0 = 0.5$ with $L_T/a = 0.1$, $T_i(s_0) = 4keV$. This configuration has a flat $\tilde{q}$ profile: $\tilde{q}_{axis} = -1.0405$, $\tilde{q}_{edge} = -1.0464$, implying that $k_{||,m}(s) \simeq const$. The magnetic gradients are rather small: $L_B/a \sim 8$ (therefore comparable to those of a tokamak of aspect ratio 8).

Simulations have been performed for various helical mode numbers n. The real frequencies ω and the growth rates γ are shown in Fig.1,left. For low n, both ω and γ increase linearly with n. A plot of the mode structure (Fig.1,right) shows a rather pure m poloidal dependence. For $n \geq 2$, $\omega > \omega_b$ and we do not expect to be in the trapped ion regime: this has been checked by artificially suppressing the $v_{||}$ and $v_{\perp}$ variation in Eq.(7) and the result is unchanged. Even for $n < 2$ we could not find a trapped ion mode, probably because of the small trapped particle fraction ($\simeq 0.25$). Therefore, for $n \leq 12$ the mode is a slab-ITG. As n is further increased, the mode structure becomes more complicated. In fact, in many cases, several modes are present in the simulation, indicating that two (or more) modes have similar γ but different ω. The interpretation of the PIC simulation results is therefore more difficult. In some cases we were able, by initializing different perturbations and shifting the frequency, to identify two competing modes. Another characteristic of the high n modes is that as n increases the mode amplitude tends to become higher in the unfavourable ∇B region (low field side). An example is shown in Fig.2,left. This behaviour is similar to that of the toroidal ITG in tokamaks. Here we have a "helical-ITG", but the mode structure does not show such a broad m spectrum as in a standard tokamak: even at high n, we do not have overlapping of several m's having resonance surfaces in the gradient region: either the whole plasma is resonant (e.g. for $m = 25, n = 24$) or it is not, because of the flat $\tilde{q}$. Another effect comes into play at high n: finite Larmor radius. For $n = 28$ we have $k_{\perp}\rho \simeq 1$ at $s = s_0$. The large damping tends to suppress the mode, and this is the reason of the decrease of γ for high n. This FLR effect is also responsible for the change in the mode localization (Fig.2,right): at high n it peaks at $s \simeq 0.6$ where T_i is smaller, whereas at low n it peaks at $s \simeq 0.4$. Thus $k_{\theta}\rho$ is nearly constant at the maximum radial mode localization, therefore ω is also nearly constant for $n > 22$.

Conclusion. These first simulations of ITG modes in a helical configuration indicate that the modes potentially creating the highest transport are slab-ITGs at relatively low n. The small ∇B and the very low shear are typical for such straight stellarators: these seem to be favourable properties to minimize ITG-based transport.

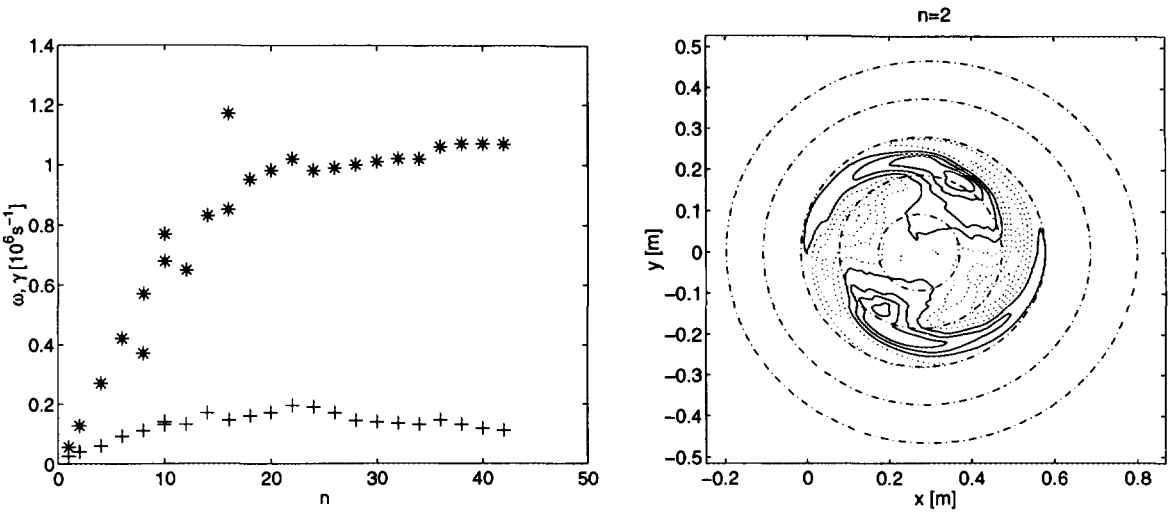

Figure 1: *Left: frequency ω (stars) and growth rate γ (crosses) as function of the helical mode number n. Right: contours of the perturbed potential ϕ for $n = 2$.*

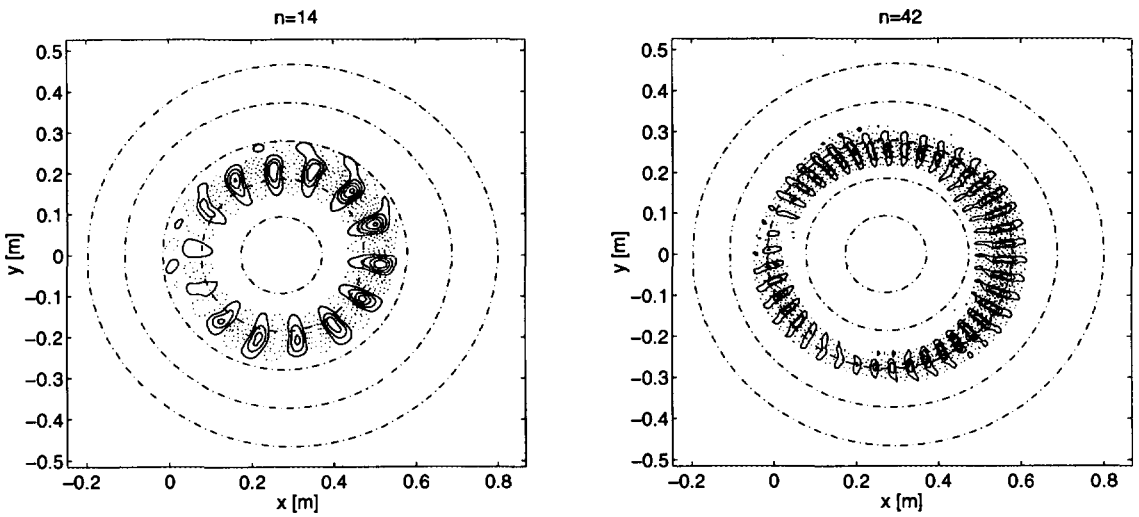

Figure 2: *Contours of the perturbed potential ϕ for $n = 14$ (left) and $n = 42$ (right) .*

Acknowledgements. This work was partly supported by the Swiss National Science Foundation. We thank W.A. Cooper and S. Brunner for helpful discussions.

References

[1] M. Fivaz, *et al.*, Theory of Fusion Plasmas, Int. Workshop, Varenna, August 1996, Editrice Compositori, Societa Italiana di Fisica, Bologna, 1997, p.485.

[2] M. Fivaz, Global ion-temperature-gradient instabilities in finite pressure tokamak plasmas, PhD Thesis no.1692(1997) EPFL, LRP 582/97.

[3] A. Bhattacharjee, *et al.*, Phys. Fluids 26 (1983) 880.

[4] N. Dominguez, *et al.*, (1992) 2894.

[5] R.E. Waltz, A.H. Boozer, Phys. Fluids B 5 (1993) 2201.

[6] M. Persson, J.L.V. Lewandowski, H. Nordman, Phys. Plasmas 3 (1996) 3720.

CH9800024

On Resonance Absorption and Continuum Damping

A. Jaun[1,2], K. Appert[1], T. Hellsten[2], J. Vaclavik[1], L. Villard[1]

[1] CRPP-EPFL, Association EURATOM-Confédération Suisse, CH-1015 Lausanne, Switzerland

[2] Alfvén Laboratory, EURATOM-NFR Association, KTH, SE-100 44 Stockholm, Sweden

ABSTRACT. The absorption of power is studied with fluid and gyrokinetic plasma models, when two Alfvén or ion-ion hybrid resonances provide for a weak damping in a partially standing wavefield. Examples chosen in slab and toroidal geometry show that the the fluid predictions based on resonance absorption are generally very different from the Landau damping of mode-converted slow waves. They in particular suggest that the continuum damping of toroidal Alfvén eigenmodes (TAE) and the power deposition profiles obtained in the ion-cyclotron range of frequencies (ICRF) using fluid plasma models are very misleading.

PACS numbers: 52.35.Bj, 52.35.Py, 52.50.Gj, 52.65.Tt

Ever since Landau's lesson, which lead to the discovery of the damping associated with the wave-particles resonance, it has been recognized that the integration over time of partial differential equation singularities requires a careful treatment that guarantees in effect that the causality remains preserved. By analogy, when the fluid wave equations are integrated in presence of an Alfvén or ion-ion hybrid resonance, a residual absorption of power appears which may be evaluated either by taking into account an arbitrarily small dissipation of the plasma or by adding artificially an imaginary part to the frequency. Studying the propagation of the fast-magnetosonic wave in the ion-cyclotron range of frequencies (ICRF), Budden [1] for example determined the fraction of the power absorbed, transmitted and reflected by a resonance-cutoff pair using a fluid plasma model, without specifying the mechanism actually responsible for the power dissipation.

If the plasma temperature is sufficiently large, the resonant layers where the fluid equations are singular coincide with the location where the fast wave energy can be converted to slow kinetic waves owing their existence to the finite Larmor radius (FLR) excursion of the ions [2]. The change of polarization accompanied with a rise in the electric field component parallel to the magnetic field is then generally responsible for the power dissipation, with resonant wave-particle interactions that occur as the slow wave propagates away from the conversion layer. Using an FLR expansion [3, 4, 5] and solving the full non-local problem [6], it has been found that the total power converted from a fast wave traveling in a single pass through a resonance depends only weakly on the slow wave parameters; the resonance absorption from fluid plasma models then coincides to a good degree of accuracy with the Landau damping of the slow wave described by the gyrokinetic models.

The aim of this letter is to draw attention to the fact that this is not in general true when two resonances are present in the same global wavefield, this even when the slow wave is damped in the vicinity of the mode conversion surface. In particular, the continuum damping of Alfvén eigenmodes (AE) [7, 8] and the resonance absorption of ICRF driven wavefields calculated with toroidal fluid plasma models [9, 10] are shown to be dramatically different from our gyrokinetic calculations, suggesting that AE mode stability threshold and ICRF power deposition profile predictions are very questionable when using fluid models.

To illustrate the concept first in a simple shearless slab plasma, Fig.1 shows an Alfvén wave heating scenario similar to the TCA tokamak [11] (B_0=1.5 T, $n_{e,0} = 2.3 \times 10^{19}$ m^{-3}, $T_{D,0}$=350 eV, $f_{ant} = 2$ MHz, $k_y = -5$ m^{-1}, $k_z = 2.9$ m^{-1}). An antenna current is imposed in the vacuum region on the right ($x = x_a = +19$ cm) and launches an evanescent fast wave into the plasma ($|x| < x_p = 18$ cm). After reflections, a global wavefield is created oscillating in phase in the entire cavity bounded by perfectly conducting walls ($|x| = x_w = 21$ cm). A parabolic variation of the density $n_e(x) = n_D(x) = n_{e,0}[1 - 0.95(x/x_p)^2]$ generates two Alfvén resonances at $|x| = x_r = 9.2$ cm, which are set to electron temperatures that differ

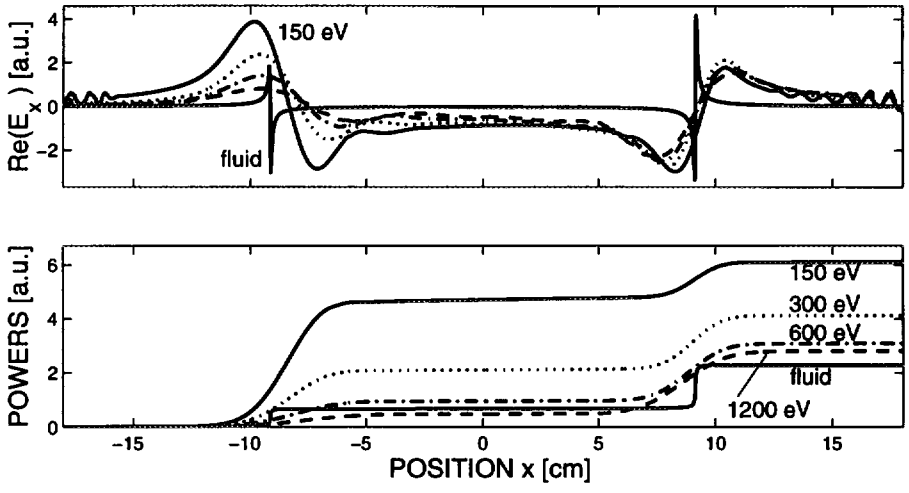

Figure 1: Alfvén wave heating scenario in a TCA-like slab plasma driven with an antenna from the right. The wavefield $Re(E_x)$ (top) and the integrated power $P(x)$ (bottom) calculated using a fluid model are compared with their gyrokinetic counterparts obtained for a rising temperature $T_{e,0}$ = 150, 300, 600, 1200 eV. The conversion layers are set to temperatures that differ by more than a factor two with an asymmetric profile of the form $T_e(x) = T_{e,0}[1 - 0.95(x/18)^2]^2[1 - 0.5(x/18)]^2$.

by more than a factor two $T_e(x) = T_{e,0}[1 - 0.95(x/x_p)^2]^2[1 - 0.5(x/x_p)]^2$, keeping that of the deuterons equal on both sides $T_D(x) = T_{D,0}[1 - 0.95(x/x_p)^2]^2$ eV. Using the full wave code ISMENE [12, 13] to compute the perpendicular wavefield (E_x, E_y) with a cold-fluid plasma model (see Ref.[13], eqs.6.1-6.2), sharp variations appear at the resonances which have been numerically resolved in Fig.1(top) by adding a small imaginary part $\delta = 0.02$ to the antenna frequency $\omega = 2\pi f_{ant}(1 + i\delta)$. Apart from details in the vicinity of the resonant layers, a change of the artificial damping $\delta \in [0.002; 0.02]$ does neither affect the integrated power $P(x) = \int_{-x_p}^{x} Im[\frac{\omega}{8\pi} Im(\mathbf{E}^* \cdot \epsilon \cdot \mathbf{E})]dx'$ in Fig.1(bottom) nor does it modify the relative power fraction absorbed at each resonance (table 1, fluid), suggesting that the power resonantly absorbed does not depend on the manner how the equations are regularized.

This fluid calculation has now to be contrasted with the gyrokinetic results from the same code, when all the wavefield components (E_x, E_y, E_z) are solved in terms of a second order FLR expansion of the plasma dielectric tensor (see Ref.[13], eqs.6.17-6.20). Fig.1(top) shows that a mode-converted kinetic Alfvén wave (KAW) propagates inwards from both sides and gets immediately damped by Landau interactions with the electrons in the neighborhood of the conversion layer. The short wavelength oscillations in the edge region ($|x| > 12$ cm) come from the surface quasi-electrostatic wave (SQEW) which is directly excited at the plasma boundary, but is unimportant for the subsequent analysis. Rising the electron temperature in the center $T_{e,0} = 150, 300, 600, 1200$ eV while keeping that of the ions fixed, Fig.1(bottom) shows that the integrated power profile $P(x)$ is changing: not only the total power absorption is mod-

$T_{e,0}$ [eV]	$f^{left}_{x=-x_r}$ [%]	$f^{right}_{x=+x_r}$ [%]
150	78	22
300	51	49
600	44	56
1200	17	83
fluid model	30	70

Table 1: Fraction of the power absorbed by each resonance, based on the fluid and gyrokinetic power deposition profiles in Fig.1(bottom)

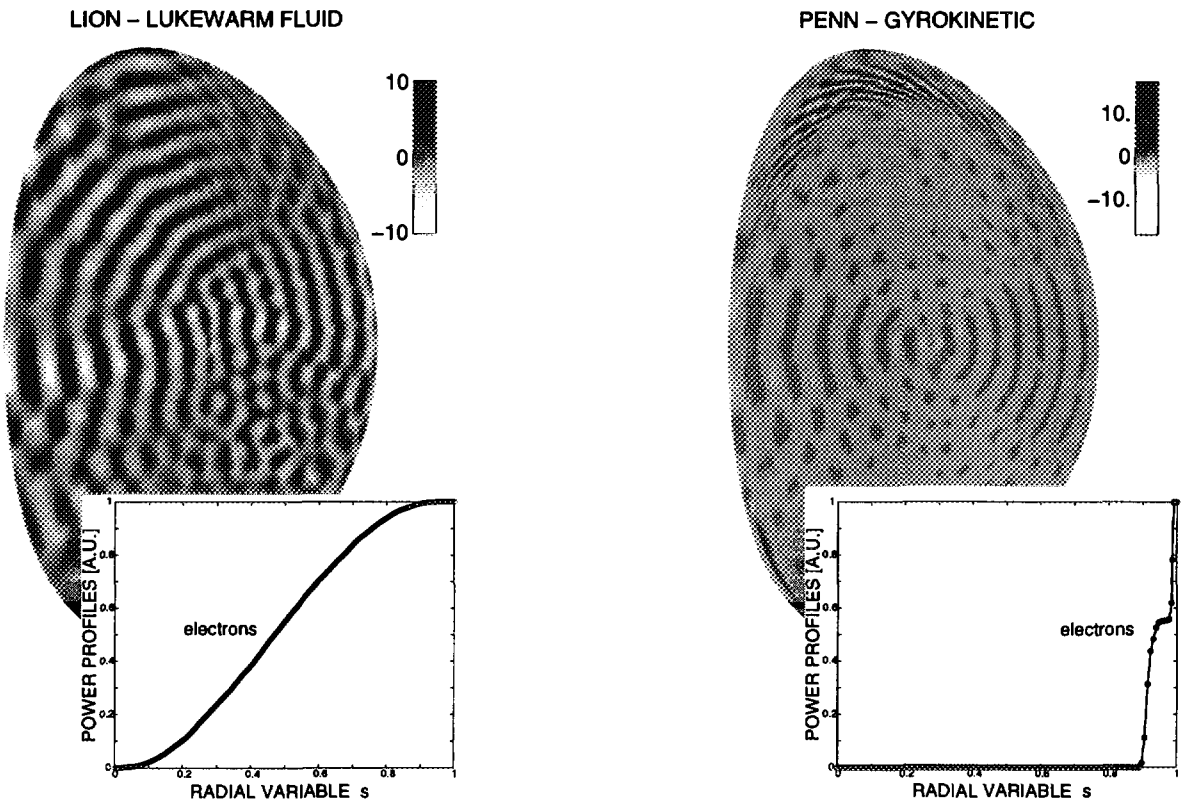

Figure 2: Current drive scenario proposed in Ref.[17] for ITER. The global wavefield $Re(E_n)$ (top) and the integrated power profile $P(s)$ (bottom) both show that the mode-conversion predicted by the gyrokinetic PENN calculation (right) is not reproduced with resonance absorption in the fluid LION code (left), suggesting that fluid predictions can be very misleading.

ified, but also the fraction absorbed by each resonance is dramatically different (table 1). This strong dependence on the temperature is of course not reproduced with the fluid plasma model and is in apparent contradiction with the small dependence on the slow wave parameters which has previously been observed in other comparisons. The paradox is solved by realizing that a small change in the "single pass" mode-conversion efficiency, which is rendered visible because of the temperature asymmetry, is here strongly amplified when the global wavefield carries fast wave energy from one resonance to the other.

This phenomenon, which has for simplicity been illustrated with the simple slab calculation above, becomes particularly important in tokamaks and stellarators where the magnetic curvature and the finite frequency in the ion-cyclotron range couple different poloidal and toroidal harmonics, forming global modes which can interact with resonant surfaces throughout the plasma radius. Alfvén eigenmodes get damped by resonances, but the continuum damping predicted using fluid plasma models [7, 8] sometimes disagrees by an order of magnitude with the gyrokinetic predictions and the experimental measurements [14, 15]. ICRF heating scenarii generally involve a multitude of resonances with large poloidal mode numbers $|m| > 20$. Global fluid calculations suggest that they are generally not excited because the geometrical coupling is very weak for low antenna mode numbers $|m_{ant}| \sim 5$. The gyrokinetic calculations from Ref.[16] however show that large poloidal mode numbers appear because of the toroidicity, when the fast and KAW wavelengths match at a resonance $\vec{k}_{fast} = \vec{k}_{slow}$ where the thermal electron velocity exceeds the parallel wave phase velocity $\omega/(k_{\|} v_{th,e}) < 1$.

The second example illustrates this in Fig.2 with a current-drive scenario proposed in Ref.[17] for the international thermonuclear experimental reactor (ITER) (B_0=6 T, $q_0 = 1.03$, $\beta_{tor} = 2.7\%$, $n_{e,0} = 1.4 n_{D,0} = 3.5 n_{T,0} = 1.4 \times 10^{20}$ m^{-3}, $T_{e,0} = T_{D,0} = T_{T,0} = 19$ keV, $f_{ant} = 20$ MHz, $n_{tor} = 21$). The lukewarm fluid LION code [9] calculation in Fig.2(left) suggests that the fast wave emmitted by an antenna on the low magnetic field side of the torus, first propagates inwards past the magnetic axis

and forms a partially standing global wavefield that extends throughout the torus. The coupling to high poloidal mode numbers is however sufficiently weak that the resonance absorption remains negligible and the power gets almost homogeneously absorbed by the fast wave electron Landau damping and transit-time magnetic pumping (TTMP). This fluid prediction is dramatically different from the gyrokinetic result obtained from the PENN code [16], which shows that strong mode-conversion takes place where the partially standing fast wavefield meets the KAW scalelength in the neighbourhood of fluid resonances with large poloidal mode numbers $m \simeq 25$. The power is then mainly deposited by the electron Landau damping of the KAW, in the plasma edge region where the resonance absorption computed with fluid plasma models remains negligible. Apart form questioning the validity of fluid plasma models for weak absorption, this mode-conversion at the plasma edge provides for a plausible mechanism explaning the degradation in the heating efficiency which has been observed in the experiments [18].

In summary, both examples chosen above in slab and toroidal geometry show that fluid plasma models cannot be used to correctly predict the power absorption and the continuum damping when two resonances or more are present in a partially standing wavefield. This is in particular true for the prediction of Alfvén eigenmode dampings and the modeling of the power deposition profiles during ICRH, where more sophisticated gyrokinetic descriptions are required - at least.

One of the authors (A.J.) acknowledges useful discussions with F. Zonca. This work was supported in part by the Swiss and the Swedish National Science Foundations and the calculations were performed on the CRAY C-94 super-computer in Linköping.

References

[1] K. Budden, *Radio Waves in the Ionosphere*, Cambridge University Press (1985) 596

[2] A. Hasegawa, L. Chen, Phys. Rev. Lett. **35** (1975) 370

[3] D.G. Swanson, Phys. Fluids **24** (1981) 2035

[4] P. Colestock, R. Kashuba, Nucl. Fusion **23** (1983) 763

[5] J.A. Heikkinen, T. Hellsten, M.J. Alva, Nucl. Fusion **31** (1991) 417

[6] O. Sauter, J. Vaclavik, Comput. Phys. Commun **84** (1994) 226

[7] M. N. Rosenbluth, H.L. Berk, J.W. Van Dam, D.M. Linberg, Phys. Rev. Lett. **68** (1992) 596

[8] F. Zonca, L. Chen, Phys. Rev. Lett. **68** (1992) 592

[9] L. Villard, K.Appert, R.Gruber, J.Vaclavik, Comput.Phys.Reports **4** (1986) 95

[10] D. Gambier, A. Samain, Nucl. Fusion **25** (1985) 283

[11] G.A.Collins, F.Hofmann, B.Joye, Phys. Fluids **29** (1986) 2260

[12] K.Appert, T.Hellsten, J.Vaclavik, L.Villard, Comput. Phys. Commun. **40** (1986) 73

[13] J. Vaclavik, K. Appert, Nucl. Fusion **31** (1991) 1945

[14] A. Jaun, A. Fasoli, W.W. Heidbrink, Phys. Rev. Lett., submitted

[15] A. Fasoli, J. Lister, J.-M. Moret, S. Sharapov, D. Borba, G. Bosia, D. Campbell, J. Dobbing, C. Gormezano, J. Jacquinot, P. Lavanchy, Ph. Marnillod, A. Santagiustina, Phys. Rev. Lett. **75** (1995) 645

[16] A. Jaun, K. Appert, J. Vaclavik, L. Villard, Comput. Phys. Commun. **92** (1995) 153

[17] *Fast Wave Heating and Current Drive in ITER*, Eur. Coord. Comm. on Fast Wave Current Drive and Heating (CCFW), edited by V. Bhatnagar, J. Jacquinot, NET Report EUR-FU/XII/163/94 (1994)

[18] L.-G. Eriksson, T. Hellsten, Nucl. Fusion **29** (1989) 875

CH9800025

COMPARISON OF HIGH CURRENT DISRUPTION LIMIT IN ELONGATED PLASMAS IN TCV WITH IDEAL AND RESISTIVE MHD MODELS†

O. Sauter, F. Hofmann, H. Reimerdes, I. Furno, R. Behn, M. J. Dutch, Y. Martin, J.-M. Moret, C. Nieswand, Z. A. Pietrzyk, A. Pochelon

Centre de Recherches en Physique des Plasmas
Association EURATOM-Switzerland
PPB - Ecublens, 1015 Lausanne, Switzerland

Abstract

Elongated plasmas up to κ=2.5 have been obtained in the Lausanne Tokamak TCV[1]. For $\kappa < 2.3$, the normalized current limit, I_N=I[MA]/a[m]B[T], increases with elongation and is limited by the standard ideal limit at q_a=2. However for κ>2.3, a disruption occurs at larger values of $q_a(\kappa)$, such that the current limit stays about constant at $I_N \approx 3$[1]. The modes observed at the disruption are typically m/n=2/1 and 3/2 modes. The observed disruption limit is consistent with the prediction of the n=1 ideal MHD limit presented in Ref.2 for analytical plasma shapes. We have computed the ideal and resistive MHD limit for the actual experimental plasma shapes and profiles. We find that the shots which disrupted are indeed very close to the ideal n=1 external kink β-limit. We also see that, including resistivity, the 4/3, 3/2 and 2/1 modes are unstable even well below this limit, which agrees with the experimental data. For $2.5<\kappa<3$, we have varied the profiles over a wide range and our results confirm the prediction of Refs.2 and 3, which is that only by keeping q_a just above 3 and decreasing the plasma inductance, l_i, one can find stable configurations.

Introduction

The upper β-limit, $\beta = 2\langle p \rangle_{vol}/\mu_0 B_0^2$, in an axisymmetric plasma is determined by the ideal MHD limit and is quite well described by the Troyon limit[4]:

$$\beta\ [\%] = c_T\, I_N = c_T\, I\ [MA] / (a\ [m]\ B\ [T]) \qquad (1)$$

The effective value of the Troyon factor c_T is typically around 2.5 to 4 depending on the pressure and current profiles. The β-limit described by Eq.(1) is not valid for reversed shear profiles, where plasma rotation and wall stabilization effects are necessary to obtain stable high-β plasmas. At very high elongation, which maximizes the plasma current for a given minor radius a, and near the plasma current limit, Eq.(1) is not valid either as has been shown in Ref.2. Therefore, to determine how much we can really increase β when increasing the elongation κ is one of the main objectives of the TCV experiment (Tokamak Configuration Variable)[5]. In the last campaign, highly elongated discharges (κ>2.3) have been obtained, many of which disrupted when approaching a given normalized current $I_N \approx 3.05$[1], close to the prediction of Ref.2. In this work, we compute the ideal and resistive β-limits using the plasma shape and profiles of TCV discharges. As is shown below, we recover the results of Ref.2, and those of Ref.3 for higher κ. Moreover we find that the 4/3, 3/2 and 2/1 modes are the most unstable resistive modes, in agreement with experimental data.

Experimental results and comparison with numerical results

The experimental high elongation discharges are summarized in Figs.1 and 2. For κ=2.3, the theoretical current limit, at zero β, is equal to $I_N \approx 2.85$,

†This Work is supported in part by the Swiss National Science Foundation

determined by $q_a \geq 2$. However at higher elongation all discharges disrupt for $I_N \geq 3$. This had already been predicted[2] at the time when TCV was designed, as shown by the solid lines in Fig.1. In that case, two plasma shapes were analyzed in more detail at $\kappa=2.5$, a Racetrack and a D-shaped plasma. We see that the β-limit does follow Eq.(1) at low I_N, however decreases much below the $q_a=2$ limit. As the discharges in Fig.1 are all in ohmic regime, β is not a free parameter and is typically around 2.5% as seen in Fig.1. Therefore the experimental points are near the D-shape limit, even though the actual shape is closer to a Racetrack, with however a non-negligible triangularity.

We have studied in more detail two shots at $\kappa \approx 2.5$, one which did not disrupt, 12413, and one which did disrupt, 12414. The time traces are shown in Fig.3, where one sees that, in the shot 12414, first a 4/3 mode occured, causing a minor disruption, then a 3/2 and finally a 2/1 mode locked and caused the disruption. This sequence is typical with or without the occurence of the 4/3 mode. In the shot 12413, two 4/3 modes occured, causing two minor disruptions, as seen on the SXR measurement, but as no 2/1 mode appeared the discharge survived. One can see that κ, I_N and β were all slightly lower in the shot 12413. These two discharges are quite typical of high elongation ohmic discharges.

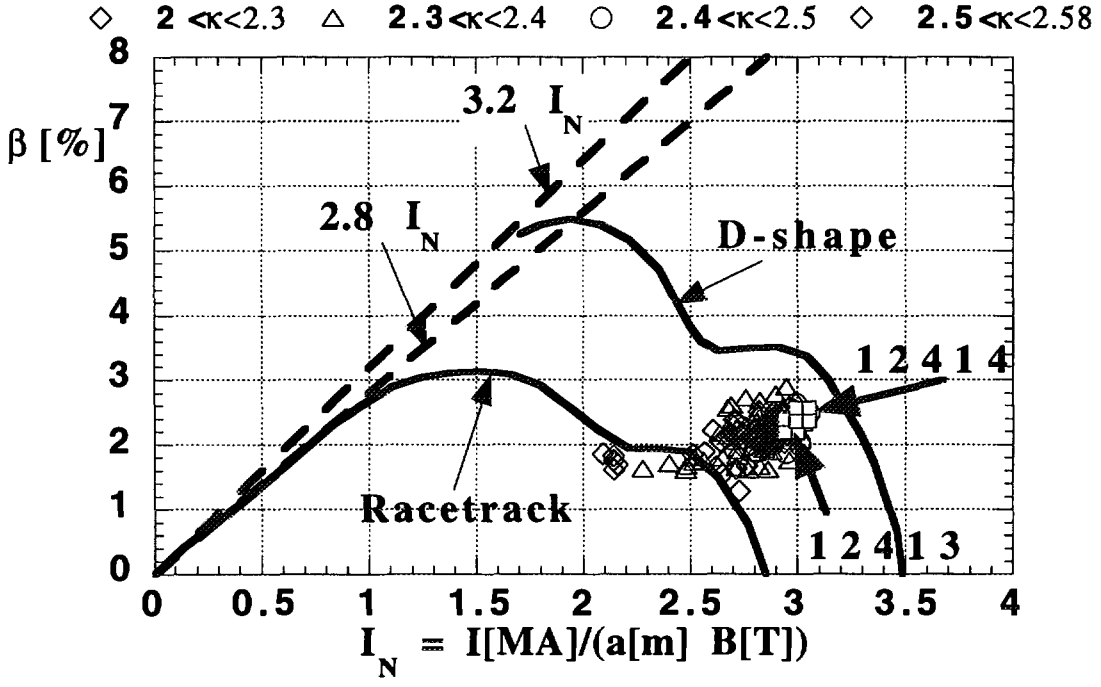

Fig.1: Ideal limit for a D-shaped and a Racetrack plasmas as in Fig.4 of Ref.2. The symbols show TCV results for $\kappa>2$.

The equilibria 12413 at t=0.76s and 12414 at t=0.794s have been reconstructed using LIUQE[6] and coupled to the equilibrium code CHEASE[7]. Then we have used ERATO[8] and KINX[9] to study the ideal limit, and MARS[10] and a cylindrical Δ' calculation to study the resistive MHD modes. All these codes are coupled to CHEASE. As q_a is relatively low, to have stable n=0 plasmas, the inversion radius is relatively large. Therefore it is difficult to separate the stability limit of the internal 1/1 kink mode from the external kink limit. This is why we have flattened the q profile such as to keep $q \geq 1.05$ everywhere, while keeping l_i equal to the experimental value ($\approx$0.6-0.65). Note that the central q profile is not accurately measured in TCV. Therefore we have varied the current and

pressure profiles, around the experimental profiles, to take into account experimental uncertainties. For both the 12413 and 12414 discharges we find the same ideal β-limit, shown as a hatched region in Fig.2. The marginal β is not a line as it depends slightly on the profiles. We see that the shot 12414, as well as all the shots with $I_N \geq 3$ which disrupted, are very close to the ideal limit, whereas the shot 12413 is further away, consistent with the experiment. However the modes grow on a resistive time-scale and we have checked that the ballooning and n=2, n=3 kink β-limits are much higher.

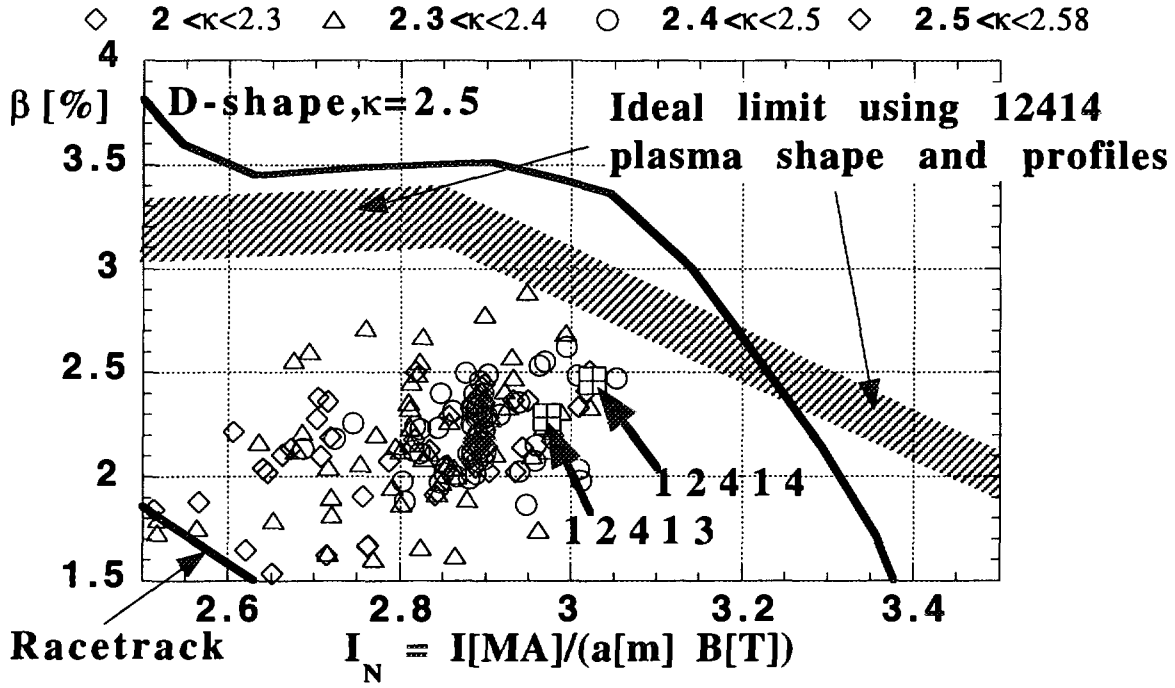

Fig.2: The symbols show TCV results for different elongation. All shots with $I_N \geq 3$ disrupted. The hatched region represents the ideal marginal limit, while the region underneath is unstable to resistive modes.

Therefore we have analyzed these equilibria with the resistive MHD code MARS and found both the 12413 and the 12414 discharges unstable to n=1, 2 and 3, with the largest growth rate for the n=1 mode consistent with the experiment. The resistive unstable region, in Fig.2, is the whole region underneath the ideal limit down to very low β as it depends mainly on the current profile. We have also computed the Δ' values, using the experimental q profiles and a cylindrical approximation. We find the 4/3, 3/2 and 2/1 unstable, whereas the other modes, e.g. 5/4, 5/2, 4/2 and 3/1, are stable. This is consistent with the experiment, as in all the discharges analyzed so far, only 4/3, 3/2 and 2/1 modes have been observed.

In order to increase the operational space, we tried to change the plasma shape and to use different current profiles, reversed shear and low l_i. We find, as first mentioned in Ref.2 and confirmed in Ref.3, that only by keeping $q_a \geq 3$ fixed and reducing I_N as much as possible, one obtains stable configurations for κ up to 3. This reduces l_i and is therefore good for the n=0 stability as well, but reduces the β-limit to a value below 2-3%. The optimal current profiles are very similar to profile (c) in Fig.3a of Ref.2, such that one has finite shear in the center and low shear up to the q=2 surface and l_i is below 0.5. These types of current profiles

will probably require the help of the ECRH system, which is now available on TCV, in order to be able to obtain stable κ=3 discharges.

Conclusion

We have shown that the high elongation, κ>2.3, discharges in TCV which disrupt are at or very close to the ideal MHD limit. We have also shown that the modes occuring just before the disruption or causing minor disruptions are conventional resistive modes, even though the modes with large island width can be further destabilized by the neoclassical perturbed bootstrap current. In order to reach elongations larger than 2.5, while remaining vertically stable, one will need to control the current profile to decrease l_i below 0.5.

References

1. F. Hofmann et al, in Proc. of the 24th EPS Conference, Berchtesgaden, Germany, June 1997.
2. A. D. Turnbull et al, Nucl. Fus. 28 (1988) 1379.
3. G. Eriksson et al,Plasma Phys. (Proc. 1992 Int. Conf. Innsbruck) 16C, Part I, EPS(1992) 343.
4. F. Troyon et al, Plasma Phys. Controll. Fus. 26 (1984) 209.
5. F. Hofmann et al, Plasma Phys. Control. Fusion **36** (1994) B 277.
6. F. Hofmann et al, Nucl. Fus. **28** (1988) 1871.
7. H. Lutjens et al, Comput. Phys. Commun. **97** (1996) 219
8. R. Gruber et al., Comput. Phys. Commun. **21** (1981) 323.
9. L. Degtyarev et al, Comput. Phys. Commun. **103** (1997) 10.
10. A. Bondeson et al, Phys. Fluids B **4** (1992) 1889.

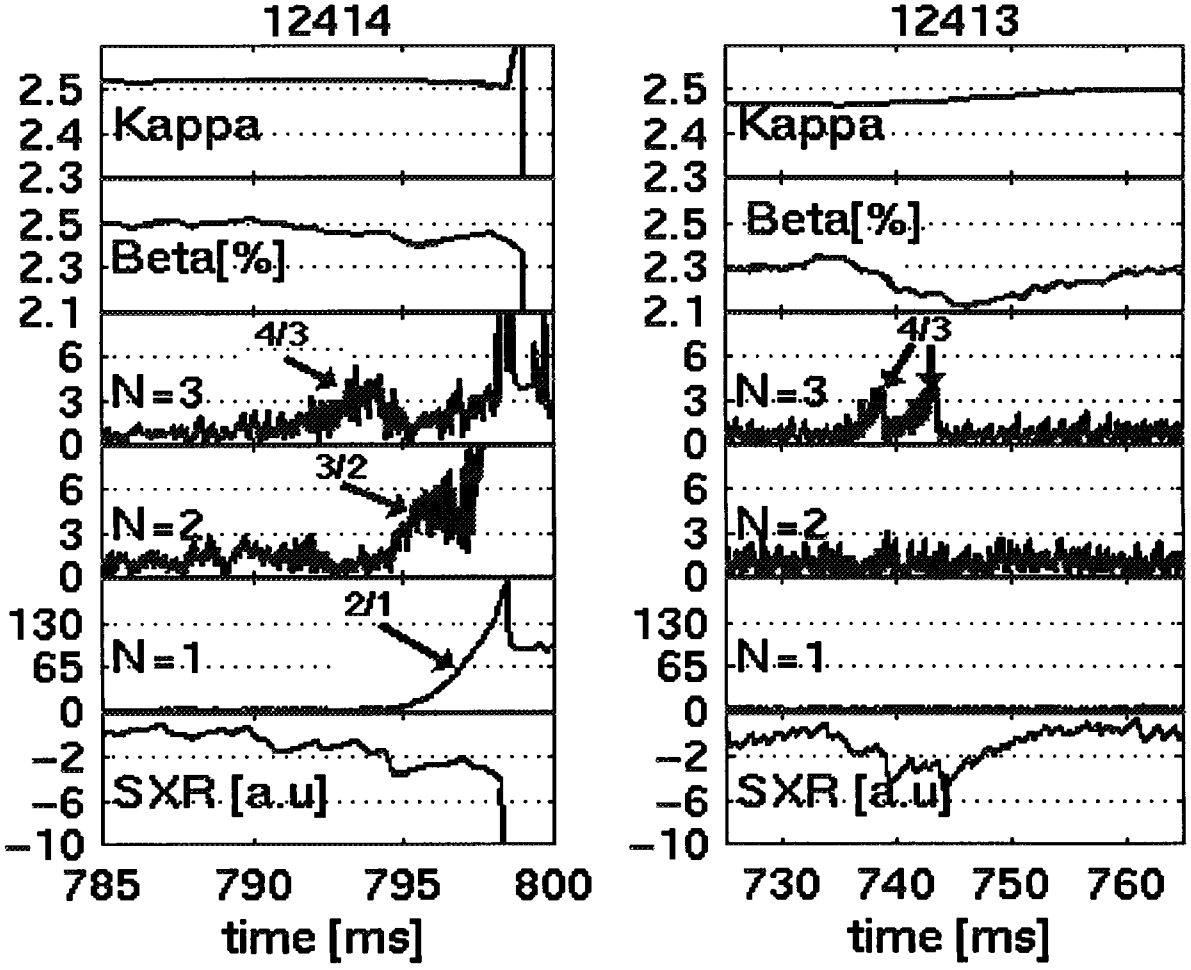

Fig.3: Time traces for shots 12414 and 12413. The 12414 disrupted due to a 2/1 locked mode very near the ideal limit, as shown in Fig.2.

CH9800026

Ideal MHD stability of plasmas with toroidal, helical and vertical field coils

A. Ardelea, W.A. Cooper
Centre de Recherche en Physique des Plasmas (CRPP/EPFL), Association Euratom-Confederation Suisse, Lausanne, Switzerland

Abstract: A simple configuration consisting in a set of toroidal, helical and vertical field coils is used to calculate free boundary equilibria with nonzero plasma current and approximately helical plasma boundary. The amount of helical boundary deformation is controlled by the ratio of the current in the helical field coils to the current in the toroidal field coils. When this ratio is increased the $(m,n) = (2,1)$ external kink is stabilized at $\beta \simeq 1\%$ for inverse rotational transform profiles in the region $q < 2$.

1. Introduction

In a previous work [1], we investigated the global ideal magnetohydrodynamic (MHD) stability of plasmas with a prescribed (fixed) helical boundary deformation and non vanishing toroidal current with respect to the (m,n) external kink modes $n = 1,2,3$ and $m = n+1$. $L = 2$, 3 single helicity and mixtures (of both) configurations were studied by systematically varying parameters such as the type and amount of helical boundary deformation, the aspect ratio, the number of equilibrium field periods, the toroidal current density and the pressure profiles. Once these parameters were fixed, sequences of equilibria differing in the amount of helical boundary deformation and such that $1 \leq q \leq 2$, were calculated with the fixed boundary version of the VMEC [2] code. The stability analysis was performed with the TERPSICHORE [3] code. It was shown that increasing the helical boundary deformation leads to the stabilization of (m,n) external modes with $n = 1,2,3$, $m = n+1$ at values of $\beta \simeq 1 - 2\%$. These modes are unstable in the circular tokamak at the same value of β. If δ is a measure of the plasma boundary deformation, then windows of stability $[\delta_{min} \quad \delta_{max}]$ may exist and depend strongly on the equilibrium parameters.
We reconsider here the study of the $(2,1)$ mode with equilibria calculated with a free boundary code. The aim is twofold:
1) to test how difficult it is to obtain free boundary equilibria with single helicity bounadry deformation at nonzero plasma current and positive β.
2) to check the results of the fixed boundary calculations in the sense that we search for stability windows when the amount of current in the helical coils is monotonously increased.

2. Equilibrium calculations

The calculations of the free boundary equilibria was performed in several steps. First, a system of coils producing a toroidal (TF), a vertical (VF) and a helical field (HF) is designed; the helical conductors are wound on a torus according to the following winding law

$$v = \frac{1}{N_{per}}(\tilde{u} + \alpha sin(\tilde{u})) - \frac{l}{L}\frac{2\pi}{N_{per}} \qquad \tilde{u} = u + 2\pi\frac{l-1}{L} \tag{1}$$

with u and v the geometrical poloidal and toroidal angles of a particular coil segment, N_{per} the number of field periods, $l = 1,..L$ an index specifying a particular coil and α the pitch modulation coefficient of the helical coils. The magnetic field $\vec{B}$ is determined from the Biot-Savart law and a field line tracing code is used to find the coil geometrical parameters and currents such as to obtain closed helical flux surfaces in vacuum. The field produced by these external currents is given then as input to the free-boundary version of the equilibrium code VMEC [4]. At finite β and nonzero

plasma current, the plasma cross section is distorted; the currents in the coils are adjusted until the plasma cross section recovers an approximate helical shape.
Several types of coils systems (stellarator-, heliotron- and torsatron-like) were considered. We illustrate the results with the example of a L=2 stellarator-like configuration ($N_{per} = 4$) with 16 TF coils two piars of 2 HF coils and one pair of VF coils. Sequences of equilibria were calculated with the following parameters

$$R_0 = 5.0\,[m] \;\; r_t = 1.8\,[m] \;\; r_h = 1.4\,[m] \;\; r_v = 7.0\,[m] \;\; z_v = \pm\, 2.1\,[m] \;\; \alpha = -0.150$$
$$I_t = -1.6 \times 10^5 [A] \quad I_v = 1. \times 10^4 [A] \qquad (2)$$
$$\beta = 1\% \text{ , parabolic pressure profile , } J'(s) \sim (1 - s^{20})^8$$

The subscripts $_t$, $_h$ and $_v$ refer to the TF, HF and VF coils respectively, R_0 is the major radius, r and z are the coils radii and verical positions, I refers to the coils currents and J' is the toroidal plasma current density. The equilibria belonging to one particular sequence differ in the amount of HF coil current I_h. The coil system is illustrated in Fig.1 and plasma cross sections for two values of I_h are shown in Fig.2. In this case the plasma current was $J = 1.27 \cdot 10^5 [A]$. If the conventional (tokamak) definition of normalized beta $\beta_N = \beta / I_N$ with $I_N = J\,[MA]/(a\,[m]\; B_0\,[T])$ where a and B_0 are the averaged minor radius and the magnetic field intensity on the axis respectively, is used we obtain $\beta_N \sim 4 - 6$.

3. Stability calculations

Let $(m_e, N_{per} n_e)$ and (m_l, n_l) represent the Fourier components in Boozer coordinates (TERPSICHORE) of the equilibrium and perturbation quantities respectively. As the equilibrim configurations has several field periods, a partial decoupling of the perturbation components occurs, depending on the values of the toroidal mode numbers. The coupling between two perturabtion components (m_{l1}, n_{l1}) and (m_{l2}, n_{l2}) is nonzero if the following relations hold between the mode numbers: $[1] m_e = m_{l1} \pm m_{l2}$ and $N_{per} n_e = n_{l1} \pm n_{l2}$. This means that the perturbation toroidal mode numbers are distributed in families of non-interacting modes.
If the mode studied is $(m, n) = (2, 1)$ and if $N_{per} = 4$, the contribution of the coupling $(m_e, N_{per} n_e) \times (2, 1) \times (m_l, n_l)$ to the potential energy δW_p is nonzero only if $n_l = 3, 5, 7, 9$, etc. When the numerical study is carried in the parameter region corresponding to $1 \leq q(s) \leq 2$, then a particular attention should be given to those (m_l, n_l) perturbation components which are resonat i.e. $m_l > n_l > n = 1$. Depending on the q profile, these components can be destabilized and could lead a priori to important couplings with $(2, 1)$. The contribution of a particular $(m_{l1}, n_{l1}) \times (m_{l2}, n_{l2})$ coupling to δW_p is determined by the amplitude $A^{eq}_{me,ne}$ of the $(m_e, N_{per} n_e)$ equilibrium coupling term - c.f. [1]. Typical equilibrium quantities appearing in these couplings are $\sqrt{g}_{m_e, n_e}$ (the Jacobian), $|B^2|_{me,ne}$ and in general combinations between the coefficients of the metric tensor [5]. If $N_{per} = 4$ the coupling between $(2, 1)$ and (m_l, n_l) resonant components with $n_l = 3, 5$ requires $(m_e, N_{per} n_e)$ components with $n_e = 1$ and $m_e > 4$; the coupling with resonant (m_l, n_l) having $n_l = 7, 9$ requires $n_e = 2$ and $m_e > 8$.
The systematic study performed in [1] for fixed helical boundary shapes, showed that the $A^{eq}_{me,ne}$ amplitudes of the $(m_e, N_{per} n_e)$ components involved in couplings between $(2, 1)$ and resonant (m_l, n_l) are negligible (compared to the dominant equilibrium components) for any equilibrium quantity ($\sqrt{g}_{m_e, n_e}$, $|B^2|_{me,ne}$, etc) and for any boundary deformation δ. If the free boundary equilibrium has an approximate helical boundary shape, the above mentioned property remains valid - see Fig.3. Thus, the study of a particular mode would not require the inclusion in the calculations of the resonant perturbation components (n and $n_l \in$ the same family). This hypothesis was verified in the sense that the ratio of any of the $(m, n) \times (m_l, n_l)$ coupling contributions ((m_l, n_l) resonant) to δW_p to the dominant contributions to δW_p is very weak i.e. $\leq 10^{-4}$.
At the beginning of the equilibrium sequence presented in Fig.4 i.e for $I_h = 0.6 \times \bar{1}0^5\,[A]$ the q profile

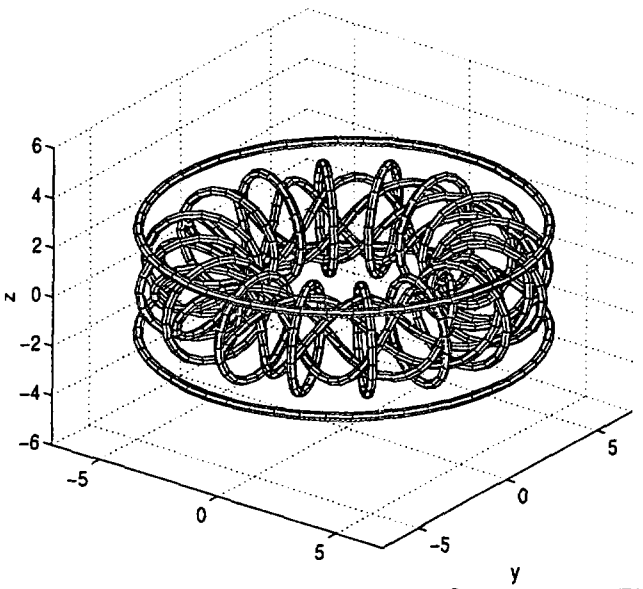

Figure 1 : *stellarator-like configuration with 16 TF coils, two pairs of 2 HF coils and one pair of VF coils*

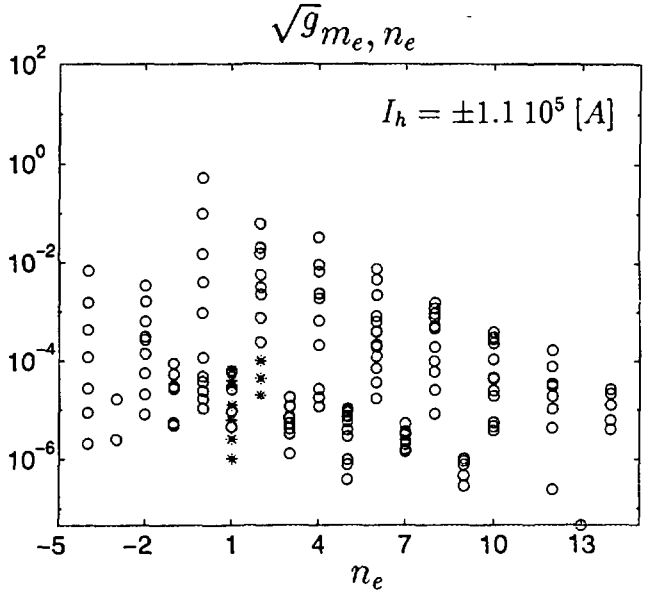

Figure 3 : $\sqrt{g}_{m_e,n_e}$ *amplitudes for the free boundary equilibrium described by Eq.(2) The x-axis corresponds to the* n_e *equilibrium mode number. The points marked with '*' represent the equilibrium components responsible for couplings between the* $(2,1)$ *mode and the* (m_l, n_l) *perturbation components with* $m_l > n_l > 1$ *(only the* $n_e \leq 2$ *i.e.* $n_l \leq 9$ *are shown). All other equilibrium components are marked with 'o'.*

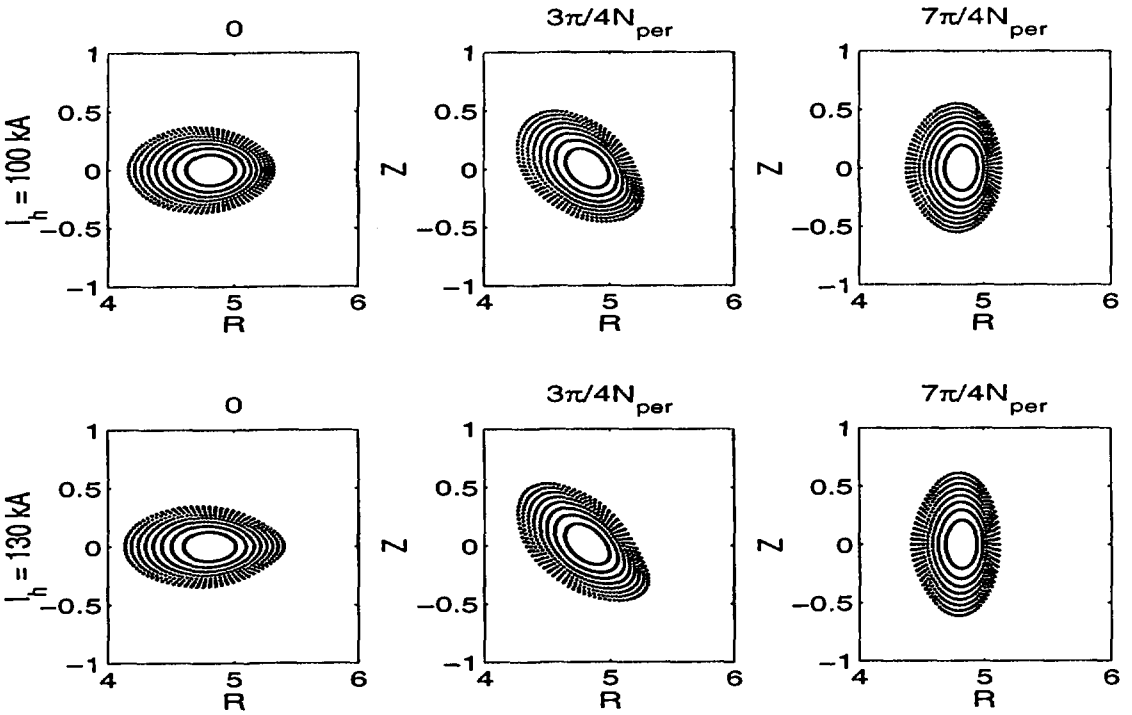

Figure 2 : *Free boundary equilibrium flux surfaces produced with VMEC. Each column represents the cross sections at one toroidal angle and each of the two rows are associated with one value of* I_h. *The coil system is represented in* Figure 1. *The equilibrium parameters are those of Eq.(2); the two equilibria correspond to the points just before and just after the stability window in Fig.4*

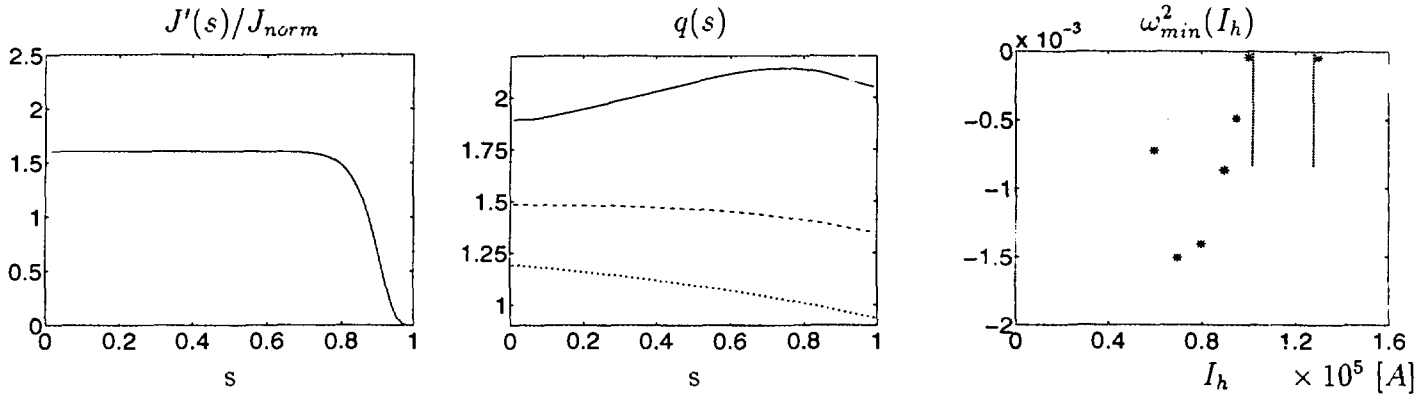

Figure 4 : *Study of the (2,1) mode:* (a) *plasma current density profile,* (b) $q(s)$ *profile,* (c) *sequence of most unstable eigenvalues* $\omega^2_{min}(I_h)$ *when the coil geometry and plasma parameters are given by Eq.(2) and the lines that follow. The aspect ratio is* $1/\epsilon \simeq 10$ *and the toroidal plasma current is* $J = 1.27 \cdot 10^5[A]$. *The inverse rotational transform profile is represented for* $I_h = 0.60 \times 10^5 A$ *(-),* $1.0 \times 10^5[A]$ *(- -) and* $I_h = 1.30 \times 10^5[A]$ *(·). The stability window is delimited by the two vertical lines and is associated with values of* I_h *between* $1 \times 10^5[A]$ *and* $1.3 \times 10^5[A]$

is such that the $(2,1)$ component is already destabilized. The effect of increasing I_h is to lower the inverse rotational transform. The $(2,1)$ component is strongly destabilized and becomes the dominant perturtbation component - we speak then about the $(2,1)$ mode. The most unstable eigenvalue $\omega^2_{min}(I_h)$ decreases until a minimum is attained, after which it starts increasing again; this is the stabilizing effect associated with an increasing (near)helical boundary deformation. Depending on the equilibrium parameters, a stability window $I_{stb} = [I_h^{min}, I_h^{max}]$ may appear in the sense that all $(m,1)$ components with $m > 1$ are stable and the $(1,1)$ component is not yet destabilized. Fig.4 (c) illustrates a stability window bounded by $I_h^{min} \simeq 1.0 \times 10^5[A]$ and $I_h^{max} \simeq 1.3 \times 10^5[A]$.
When the resonant perturbation components i.e. $(m_l, 3)$ with $m_l > 3$, $(m_l, 5)$ with $m_l > 5$, etc are taken into account and the stability calculations are performed again for those equilibria in the stable window, then several unstable eigenvalues may appear for each $I_h \in I_{stb}$. Each of these eigenvalues is associated to one of the resonant (m_l, n_l) modes (component whith largest amplitude). We systematically checked each of the $(2,1) \times (m_l, n_l)$ and $(1,1) \times (m_l, n_l)$ coupling contribution to δW_P and found that they are indeed negligible i.e. $< 10^{-4}$ compared to the dominant contributions.

4. Aknowledgements

This work was partly supported by the Swiss National Science Foundation.

References

[1] A.Ardelea, W.A.Cooper, "External kinks in plasmas with helical boundary deformation and non zero toroidal current", to appear in Physics of Plasmas, (scheduled for Oct. 1997)

[2] S.P.Hirshman, U.Schwenn, J.Nührenberg, J. Comput. Phys. **87**, 396, (1990)

[3] D.V.Anderson, W.A.Cooper, R.Gruber, S.Merazzi, U.Schwenn, Int. J. Supercomp. Appl. **4**, p.34 (1990)

[4] S.P.Hirshman, W.I.van Rij, P.Merkel, Comp. Phys. Communications, **43**, 143 (1986)

[5] W.A.Cooper, Plasma Physics and Controlled Fusion, **34**, No 6, 1011, (1992)

Canonical and magnetic coordinates applied to relativistic guiding centre drifts

W. A. Cooper

Centre de Recherches en Physique des Plasmas, Association Euratom-Confédération Suisse, Ecole Polytechnique Fédérale de Lausanne, CRPP-PPB, CH-1015 Lausanne, Switzerland

Abstract. The formulation of the guiding centre drift orbits is extended to relativistic particles in canonical coordinates with arbitrary time dependent electric and magnetic fields. The transformation to these coordinates from general flux coordinates is cumbersome for practical applications. This transformation is straightforward for Boozer magnetic coordinates which are canonical if the perturbed magnetic field is constrained to the form $\delta \boldsymbol{B} = \nabla \times (\Upsilon \boldsymbol{B})$.

A Hamiltonian formalism in canonical coordinates constitutes the most transparent and compact approach to treat the guiding centre drift orbit problem. In this paper, we extend to relativistic particles the formulation in a canonical coordinate system that is valid for arbitrary three dimensional (3D) time dependent electric and magnetic fields [1,2]. For a 3D equilibrium calculated in a different coordinate system, we demonstrate that the transformation to the canonical coordinates is too complicated for useful applications. For Boozer magnetic coordinates [3], the transformation is simple. However, the perturbed magnetic field structure cannot be arbitrary for this system to retain canonical properties.

To define canonical coordinates in a torus with arbitrary time dependent electric and magnetic fields requires that these coordinates (r, θ, ζ) satisfy the property that the vector potential and the magnetic field be expressed as [1]

$$\boldsymbol{A} = \Phi(r, \theta, \zeta, t) \nabla \theta - \psi(r, \theta, \zeta, t) \nabla \zeta \,, \tag{1}$$

$$\boldsymbol{B} = B_\theta(r, \theta, \zeta, t) \nabla \theta + B_\zeta(r, \theta, \zeta, t) \nabla \zeta \,. \tag{2}$$

where r is the radial variable θ is the poloidal angle and ζ is the toroidal angle. In other words, the coordinates are canonical when the radial components of $\boldsymbol{A}$ and $\boldsymbol{B}$ in the covariant representation vanish. As $\boldsymbol{B} = \nabla \times \boldsymbol{A}$, the magnetic field in the contravariant representation is $\boldsymbol{B} = \nabla\zeta \times \nabla\psi + \nabla\Phi \times \nabla\theta$. The canonical momenta in the drift ap-

proximation are given by $\boldsymbol{P} = p_{\|}\boldsymbol{B}/B + e\boldsymbol{A}$. The corresponding relativistic Hamiltonian is

$$H = H(\boldsymbol{p},\boldsymbol{x},t) = \sqrt{p_{\|}^2c^2 + 2\mu B m_0c^2 + m_0^2c^4} + e\chi(\boldsymbol{x},t) = \gamma m_0c^2 + e\chi(\boldsymbol{x},t)\,, \qquad (3)$$

where $\rho_{\|} = p_{\|}/eB$ is the parallel gyroradius, χ is the electrostatic potential, μ is the magnetic moment, e is the particle charge, c is the speed of light, m_0 is the particle rest mass and γ is the relativistic gamma factor. Applying the Hamiltonian formalism, we derive the equations of motion in the drift approximation [2]

$$\begin{aligned}
\dot{r} = \frac{\partial r}{\partial t} &- \frac{B_\zeta}{D}\left[\frac{\partial\chi}{\partial\theta}\Big|_{r,\zeta,t} + \frac{1}{\gamma}\left(\frac{\mu}{e} + \frac{eB}{m_0}\rho_{\|}^2\right)\frac{\partial B}{\partial\theta}\Big|_{r,\zeta,t}\right] + \frac{B_\theta}{D}\left[\frac{\partial\chi}{\partial\zeta}\Big|_{r,\theta,t} + \frac{1}{\gamma}\left(\frac{\mu}{e} + \frac{eB}{m_0}\rho_{\|}^2\right)\frac{\partial B}{\partial\zeta}\Big|_{r,\theta,t}\right] \\
&- \frac{eB^2\rho_{\|}}{\gamma m_0 D}\left(\frac{\partial\psi}{\partial\theta}\Big|_{r,\zeta,t} - \rho_{\|}\frac{\partial B_\zeta}{\partial\theta}\Big|_{r,\zeta,t} + \frac{\partial\Phi}{\partial\zeta}\Big|_{r,\theta,t} + \rho_{\|}\frac{\partial B_\theta}{\partial\zeta}\Big|_{r,\theta,t}\right), \qquad (4)
\end{aligned}$$

$$\dot{\theta} = \frac{eB^2\rho_{\|}}{\gamma m_0 D}\left(\frac{\partial\psi}{\partial r}\Big|_{\theta,\zeta,t} - \rho_{\|}\frac{\partial B_\zeta}{\partial r}\Big|_{\theta,\zeta,t}\right) + \frac{B_\zeta}{D}\left[\frac{\partial\chi}{\partial r}\Big|_{\theta,\zeta,t} + \frac{1}{\gamma}\left(\frac{\mu}{e} + \frac{eB}{m_0}\rho_{\|}^2\right)\frac{\partial B}{\partial r}\Big|_{\theta,\zeta,t}\right], \qquad (5)$$

$$\dot{\zeta} = \frac{eB^2\rho_{\|}}{\gamma m_0 D}\left(\frac{\partial\Phi}{\partial r}\Big|_{\theta,\zeta,t} + \rho_{\|}\frac{\partial B_\theta}{\partial r}\Big|_{\theta,\zeta,t}\right) - \frac{B_\theta}{D}\left[\frac{\partial\chi}{\partial r}\Big|_{\theta,\zeta,t} + \frac{1}{\gamma}\left(\frac{\mu}{e} + \frac{eB}{m_0}\rho_{\|}^2\right)\frac{\partial B}{\partial r}\Big|_{\theta,\zeta,t}\right]. \qquad (6)$$

$$\begin{aligned}
\dot{\rho}_{\|} = \frac{\partial\rho_{\|}}{\partial t} &- \frac{1}{D}\left(\frac{\partial\psi}{\partial r}\Big|_{\theta,\zeta,t} - \rho_{\|}\frac{\partial B_\zeta}{\partial r}\Big|_{\theta,\zeta,t}\right)\left[\frac{\partial\chi}{\partial\theta}\Big|_{r,\zeta,t} + \frac{1}{\gamma}\left(\frac{\mu}{e} + \frac{eB}{m_0}\rho_{\|}^2\right)\frac{\partial B}{\partial\theta}\Big|_{r,\zeta,t}\right] \\
&- \frac{1}{D}\left(\frac{\partial\Phi}{\partial r}\Big|_{\theta,\zeta,t} + \rho_{\|}\frac{\partial B_\theta}{\partial r}\Big|_{\theta,\zeta,t}\right)\left[\frac{\partial\chi}{\partial\zeta}\Big|_{r,\theta,t} + \frac{1}{\gamma}\left(\frac{\mu}{e} + \frac{eB}{m_0}\rho_{\|}^2\right)\frac{\partial B}{\partial\zeta}\Big|_{r,\theta,t}\right] \\
&+ \frac{1}{D}\left(\frac{\partial\psi}{\partial\theta}\Big|_{r,\zeta,t} - \rho_{\|}\frac{\partial B_\zeta}{\partial\theta}\Big|_{r,\zeta,t}\right)\left[\frac{\partial\chi}{\partial r}\Big|_{\theta,\zeta,t} + \frac{1}{\gamma}\left(\frac{\mu}{e} + \frac{eB}{m_0}\rho_{\|}^2\right)\frac{\partial B}{\partial r}\Big|_{\theta,\zeta,t}\right] \\
&+ \frac{1}{D}\left(\frac{\partial\Phi}{\partial\zeta}\Big|_{r,\theta,t} + \rho_{\|}\frac{\partial B_\theta}{\partial\zeta}\Big|_{r,\theta,t}\right)\left[\frac{\partial\chi}{\partial r}\Big|_{\theta,\zeta,t} + \frac{1}{\gamma}\left(\frac{\mu}{e} + \frac{eB}{m_0}\rho_{\|}^2\right)\frac{\partial B}{\partial r}\Big|_{\theta,\zeta,t}\right], \qquad (7)
\end{aligned}$$

where $D = B_\zeta\partial\Phi/\partial r + B_\theta\partial\psi/\partial r + \rho_{\|}\Big(B_\zeta\partial B_\theta/\partial r - B_\theta\partial B_\zeta/\partial r\Big)$.

Now we consider a 3D static equilibrium with nested magnetic flux surfaces. The magnetic field in the contravariant representation is $\boldsymbol{B} = \nabla\alpha\times\nabla\psi$ and in the covariant representation is $\boldsymbol{B} = \nabla\eta + \beta\nabla s$ where $\alpha = \zeta - q(s)[\theta + \lambda(s,\theta,\zeta)]$, $\eta = \mu_0[J(s)\theta - I(s)\zeta + Q(s,\theta,\zeta)]$ and $\beta = \mu_0[I'(s)\zeta - J'(s)\theta - \nu(s,\theta,\zeta)]$, where $q(s)$ is the inverse rotational transform, $2\pi I(s)$ and $2\pi J(s)$ are the poloidal and toroidal current fluxes, respectively. The periodic function λ is determined from the condition $\boldsymbol{j}\cdot\nabla s = 0$. The periodic functions Q and ν are still unspecified. It is usually the case that a 3D equilibrium is known in a different set of coordinates (s,u,v) (calculated for example with the VMEC code) and a transformation procedure to the desired canonical coordinates

(s,θ,ζ) must be prescribed. To do this, we identify $\theta = u+h(s,u,v)$ and $\zeta = v+k(s,u,v)$ where h and k are periodic functions of the known poloidal and toroidal angles u and v, respectively. For straight field lines, $\lambda(s,\theta,\zeta) = 0$. The functions α, η and β, being scalars, are invariant with respect to coordinate transformations. From the relations for α and η, we obtain $h(s,u,v) = Q_v(s,u,v) - Q(s,\theta,\zeta) - q(s)I(s)\lambda(s,u,v)/[J(s) - q(s)I(s)]$ and $k(s,u,v) = q(s)Q_v(s,u,v) - Q(s,\theta,\zeta) - J(s)\lambda(s,u,v)/[J(s) - q(s)I(s)]$ where the function $Q(s,\theta,\zeta) = Q[s,\theta(s,u,v),\zeta(s,u,v)]$ must still be specified. Invoking the expression for β, we obtain that $\nu_c[s,\theta_c(s,u,v),\zeta_c(s,u,v)] = \nu_v(s,u,v) + J'(s)h(s,u,v) - I'(s)k(s,u,v)$ which we combine with the condition that the covariant radial component of $\boldsymbol{B}$ must vanish in the canonical coordinate system to derive the differential equation

$$\left.\frac{\partial Q_c}{\partial s}\right|_{\theta_c,\zeta_c} + \frac{J'(s) - q(s)I'(s)}{J(s) - q(s)I(s)} Q_c = \nu_v(s,u,v) + \frac{J'(s) - q(s)I'(s)}{J(s) - q(s)I(s)} Q_v(s,u,v) + q(s)\frac{I'(s)J(s) - J'(s)I(s)}{J(s) - q(s)I(s)}\lambda(s,u,v)\,. \tag{8}$$

The resolution of this equation for the transformation from an arbitrary coordinates system to canonical coordinates is an extremely cumbersome procedure that makes the applicability of this formulation virtually impractical.

Boozer magnetic coordinates [3] are defined for 3D systems in which the unperturbed magnetic field forms perfect nested magnetic flux surfaces. These coordinates are also canonical if the time dependent portion of the magnetic field is constrained to have the form [4] $\delta\boldsymbol{B} = \nabla\times[\Upsilon(s,\vartheta,\phi,t)\boldsymbol{B}]$. This form is adequate to describe that radial component of any perturbed magnetic field [4]. Furthermore, the Boozer coordinates satisfy $\lambda(s,\vartheta,\phi) = 0$ (straight field lines) and $Q(s,\vartheta,\phi) = 0$ which allows a straightforward determination of the periodic functions h and k and consequently the mapping from VMEC-like coordinates. The vector potential is $\boldsymbol{A} = \Phi(s)\nabla\vartheta - \psi(s)\nabla\phi + \Upsilon(s,\vartheta,\phi,t)\boldsymbol{B}$. The canonical momenta are $P_\vartheta = e[\Phi(s) + \rho_c\mu_0 J(s)]$ and $P_\phi = -e[\psi(s) + \rho_c\mu_0 I(s)]$ where the effective gyroradius is $\rho_c = p_{||}/(eB) + \Upsilon$ [5]. Inverting these relations, we have $s = s(P_\vartheta, P_\phi)$ and $\rho_c = \rho_c(P_\vartheta, P_\phi)$. Applying the Hamiltonian formalism, we obtain the equations of motions

$$\dot{s} = \frac{\mu_0 I(s)}{D_b}\left[\left.\frac{\partial\chi}{\partial\vartheta}\right|_{s,\phi,t} + \frac{1}{\gamma}\left(\frac{\mu}{e} + \frac{eB}{m_0}\rho_{||}^2\right)\left.\frac{\partial B}{\partial\vartheta}\right|_{s,\phi} - \frac{eB^2\rho_{||}}{\gamma m_0}\left.\frac{\partial\Upsilon}{\partial\vartheta}\right|_{s,\phi,t}\right]$$

$$+\frac{\mu_0 J(s)}{D_b}\left[\left.\frac{\partial\chi}{\partial\phi}\right|_{s,\vartheta,t}+\frac{1}{\gamma}\left(\frac{\mu}{e}+\frac{eB}{m_0}\rho_{\|}^2\right)\left.\frac{\partial B}{\partial\phi}\right|_{s,\vartheta}-\frac{eB^2\rho_{\|}}{\gamma m_0}\left.\frac{\partial\Upsilon}{\partial\phi}\right|_{s,\vartheta,t}\right], \tag{9}$$

$$\dot{\vartheta} = -\frac{eB^2\rho_{\|}}{\gamma m_0 D_b}\left[\psi'(s)+(\rho_{\|}+\Upsilon)\mu_0 I'(s)+\mu_0 I(s)\left.\frac{\partial\Upsilon}{\partial s}\right|_{\vartheta,\phi,t}\right]$$
$$-\frac{\mu_0 I(s)}{D_b}\left[\left.\frac{\partial\chi}{\partial s}\right|_{\vartheta,\phi,t}+\frac{1}{\gamma}\left(\frac{\mu}{e}+\frac{eB}{m_0}\rho_{\|}^2\right)\left.\frac{\partial B}{\partial s}\right|_{\vartheta,\phi}\right], \tag{10}$$

$$\dot{\phi} = -\frac{eB^2\rho_{\|}}{\gamma m_0 D_b}\left[\Phi'(s)+(\rho_{\|}+\Upsilon)\mu_0 J'(s)+\mu_0 J(s)\left.\frac{\partial\Upsilon}{\partial s}\right|_{\vartheta,\phi,t}\right]$$
$$-\frac{\mu_0 J(s)}{D_b}\left[\left.\frac{\partial\chi}{\partial s}\right|_{\vartheta,\phi,t}+\frac{1}{\gamma}\left(\frac{\mu}{e}+\frac{eB}{m_0}\rho_{\|}^2\right)\left.\frac{\partial B}{\partial s}\right|_{\vartheta,\phi}\right], \tag{11}$$

$$\dot{\rho}_{\|} = -\frac{1}{D_b}\left[\psi'(s)+(\rho_{\|}+\Upsilon)\mu_0 I'(s)+\mu_0 I(s)\left.\frac{\partial\Upsilon}{\partial s}\right|_{\vartheta,\phi,t}\right]\left[\left.\frac{\partial\chi}{\partial\vartheta}\right|_{s,\phi,t}+\frac{1}{\gamma}\left(\frac{\mu}{e}+\frac{eB}{m_0}\rho_{\|}^2\right)\left.\frac{\partial B}{\partial\vartheta}\right|_{s,\phi}\right]$$
$$-\frac{1}{D_b}\left[\Phi'(s)+(\rho_{\|}+\Upsilon)\mu_0 J'(s)+\mu_0 J(s)\left.\frac{\partial\Upsilon}{\partial s}\right|_{\vartheta,\phi,t}\right]\left[\left.\frac{\partial\chi}{\partial\phi}\right|_{s,\vartheta,t}+\frac{1}{\gamma}\left(\frac{\mu}{e}+\frac{eB}{m_0}\rho_{\|}^2\right)\left.\frac{\partial B}{\partial\phi}\right|_{s,\vartheta}\right]$$
$$-\frac{\mu_0}{D_b}\left[I(s)\left.\frac{\partial\Upsilon}{\partial\vartheta}\right|_{s,\phi,t}+J(s)\left.\frac{\partial\Upsilon}{\partial\phi}\right|_{s,\vartheta,t}\right]\left[\left.\frac{\partial\chi}{\partial s}\right|_{\vartheta,\phi,t}+\frac{1}{\gamma}\left(\frac{\mu}{e}+\frac{eB}{m_0}\rho_{\|}^2\right)\left.\frac{\partial B}{\partial s}\right|_{\vartheta,\phi}\right]-\left.\frac{\partial\Upsilon}{\partial t}\right|_{s,\vartheta,\phi}, \tag{12}$$

where

$$D_b = \mu_0[\psi'(s)J(s)-\Phi'(s)I(s)]\Big[1+\mu_0\rho_c[J(s)I'(s)-I(s)J'(s)]/[\psi'(s)J(s)-\Phi'(s)I(s)]\Big].$$

In conclusion, we have extended the formulation of the guiding centre drift orbits in canonical coordinates valid for arbitrary time dependent electric and magnetic fields to relativistic particles. However, the transformation from a general flux coordinate system to these canonical coordinates is too cumbersome for parctical applications. The transformation to Boozer magnetic coordinates, on the other hand, is straightforward and this coordinate system is canonical for perturbed magnetic fields constrined to the form $\delta\boldsymbol{B} = \boldsymbol{\nabla}\times(\Upsilon\boldsymbol{B})$. The relativistic guiding centre drift equations of motion are explicitly derived in this system.

References

[1] Meiss, J.D., Hazeltine, R.D., *Phys. Fluids* **B2** (1990) 2563

[2] Cooper, W.A., *Plasma Phys. Control. Fusion* **39** (1997) 931

[3] Boozer, A.H., *Phys. Fluids* **23** (1980) 904

[4] White, R.B., Chance, M.S., *Phys. Fluids* **27** (1984) 2455

[5] Boozer, A.H., *Phys. Plasmas* **3** (1996) 3297